

Volumetric Printing Across Melt Electrowritten Scaffolds Fabricates Multi-Material Living Constructs with Tunable Architecture and Mechanics

Gabriel Größbacher, Michael Bartolf-Kopp, Csaba Gergely, Paulina Núñez Bernal, Sammy Florczak, Mylène de Ruijter, Núria Ginés Rodríguez, Jürgen Groll, Jos Malda, Tomasz Jungst,* and Riccardo Levato*

Major challenges in biofabrication revolve around capturing the complex, hierarchical composition of native tissues. However, individual 3D printing techniques have limited capacity to produce composite biomaterials with multi-scale resolution. Volumetric bioprinting recently emerged as a paradigm-shift in biofabrication. This ultrafast, light-based technique sculpts cell-laden hydrogel bioresins into 3D structures in a layerless fashion, providing enhanced design freedom over conventional bioprinting. However, it yields prints with low mechanical stability, since soft, cell-friendly hydrogels are used. Herein, the possibility to converge volumetric bioprinting with melt electrowriting, which excels at patterning microfibers, is shown for the fabrication of tubular hydrogel-based composites with enhanced mechanical behavior. Despite including non-transparent melt electrowritten scaffolds in the volumetric printing process, high-resolution bioprinted structures are successfully achieved. Tensile, burst, and bending mechanical properties of printed tubes are tuned altering the electrowritten mesh design, resulting in complex, multi-material tubular constructs with customizable, anisotropic geometries that better mimic intricate biological tubular structures. As a proof-of-concept, engineered tubular structures are obtained by building trilayered cell-laden vessels, and features (valves, branches, fenestrations) that can be rapidly printed using this hybrid approach. This multi-technology convergence offers a new toolbox for manufacturing hierarchical and mechanically tunable multi-material living structures.

1. Introduction

In the quest to restore the function of damaged tissues, additive manufacturing technologies are continuously opening new avenues to better capture the complex composition and function of native biological architectures.^[1] A central characteristic of biofabrication techniques is the ability to perform the automated and accurate simultaneous placement of living cells and materials (together also termed bioinks)^[2] in custom-designed patterns. Fabrication can be performed by means of light-based printing, such as stereolithography and digital light processing,^[3,4] extrusion-based,^[5,6] droplet-based or inkjet printing,^[7–9] and fiber reinforcing technologies.^[10,11] All these technologies have their individual benefits and challenges with respect to resolution, shape-fidelity, cell-viability, compatible ranges of materials (inks or resins), and printing/processing time. Yet, while each technique excels in processing certain subsets of inks and object geometries, native biological tissues are characterized by their unique multicellular and multi-material composition, shape,

G. Größbacher, P. N. Bernal, S. Florczak, M. de Ruijter, N. G. Rodríguez, J. Malda, R. Levato
Department of Orthopaedics
University Medical Center Utrecht
Utrecht University
Utrecht 3584 CX, The Netherlands
E-mail: r.levato@uu.nl

M. Bartolf-Kopp, C. Gergely, J. Groll, T. Jungst
Department of Functional Materials in Medicine and Dentistry
Institute of Functional Materials and Biofabrication (IFB), KeyLab
Polymers for Medicine of the Bavarian Polymer Institute (BPI)
University of Würzburg
Pleicherwall 2, 97070 Würzburg, Germany
E-mail: tomasz.juengst@uni-wuerzburg.de
J. Malda, R. Levato
Department of Clinical Sciences
Faculty of Veterinary Medicine
Utrecht University
Utrecht 3584 CT, The Netherlands

 The ORCID identification number(s) for the author(s) of this article can be found under <https://doi.org/10.1002/adma.202300756>

© 2023 The Authors. Advanced Materials published by Wiley-VCH GmbH. This is an open access article under the terms of the Creative Commons Attribution License, which permits use, distribution and reproduction in any medium, provided the original work is properly cited.

DOI: 10.1002/adma.202300756

and hierarchical architecture, with features from the submicron to the macroscale. Most importantly, both mechanical and biological functions are intimately correlated to this multiscale, multi-material hierarchy.^[1] New directions in the biofabrication field hold the promise to bridge this gap by converging different (and previously incompatible) bioprocessing technologies,^[12,13] with the aim to produce engineered tissue constructs that, by combining their benefits and range of achievable prints, better mimic salient features of their native counterparts, to eventually restore and replace damaged tissues.

Volumetric printing (VP) is a recently developed biofabrication technology to sculpt hydrogels into free-form 3D structures.^[14] In VP, a hydrogel with the addition of a photo-crosslinking agent is placed in a rotating platform and a light source (i.e., a laser), in combination with a spatial light modulator (such as a digital micromirror device (DMD)), is subsequently used to deliver a sequence of filtered tomographic back-projections onto this volume. The sum of the different projections rapidly generates an anisotropic, 3D light-dose distribution within the build volume, thereupon activating the polymerization reaction only in correspondence to the desired object.^[15] This process is extremely fast (<30 s to produce several cm³ parts)^[16] compared to conventional extrusion-based printing (20 min), while offering equal or greater resolution (40–200 μm) with higher spatial freedom.^[14,15] Although promising, the materials used with volumetric printing are hydrogels, which are intrinsically soft, while most tissues in the body also need to account for mechanical stability and load-bearing capacity. Techniques to mechanically stabilize soft hydrogels include the formation of interpenetrating polymer networks, the inclusion of nanoparticles, or the inclusion of fibrous reinforcements, such as structures produced via fused deposition modeling, electrospinning, and melt electrowriting (MEW).^[17] In particular, MEW generates (sub-)micrometer-scale fibers by applying a high voltage to the polymer melt. Fibers are deposited onto a moving collector plate, allowing for control over fiber deposition and subsequent scaffold architecture.^[17,18] Scaffolds made with MEW have proven to facilitate cell alignment,^[19] and increase the mechanical stability of tissue-engineered constructs.^[20] This technique is compatible with printing a variety of thermoplastic materials,^[21,22] whose biochemical composition can further be modified post-writing with surface coatings.^[11,21,23] Recently, first steps have also demonstrated the possibility to print hydrogel-based fibers.^[24] Notably, fiber deposition can be done on a flat collector plate but also on a mandrel for the fabrication of intricate tubular scaffolds.^[25–27] Tubular geometries are of particular interest for biological applications, as they recur in many tissues, and can therefore be applied as scaffolds for blood vessels, airways, intestinal and tubular kidney structures,^[28] among others.^[26,27]

One of the drawbacks of MEW tubular scaffolds is that the inclusion of cells is generally done post-printing, either by direct seeding on top of the fiber strands, or by casting with a hydrogel carrier.^[29–31] Promising composite structures have been produced, exploiting the unique ability of MEW to provide mechanical reinforcement to other cell-carrying materials.^[32] However, since the cell-laden compartment can only be loaded in simple geometries following the electrowritten mesh pattern, replicating complex, branched, and tortuous geometries typical of native tissues remains challenging.

In this work, we demonstrate for the first time the convergence of volumetric bioprinting with MEW, to pattern multiple materials and cell types in any custom-desired geometry even within opaque polymeric microfibrillar thermoplastic meshes. In shaping these novel hydrogel-cell-microfiber composites, as a proof-of-concept to demonstrate the applicability and versatility of this technology, we built a broad array of constructs that mimic key features of native blood vessels. The intricacy in design ranges from multi-branched structures to multi-cellular and fenestrated, structurally reinforced scaffolds with tunable mechanical properties, and cell-laden architectures not possible with previously existing techniques alone.

2. Results and Discussion

The convergence of different 3D printing technologies has become a widely studied concept in the fields of biofabrication and tissue engineering, given the potential to exploit the advantages of different technologies to combine different classes of materials in a single object, and to create living, hierarchical structures.^[12] In the present study, we aim to elucidate the potential and advantages offered by the convergence of volumetric printing, which allows the fabrication of highly complex, centimeter-scale structures using hydrogel-based bioresins,^[14] and MEW, which allows the creation of highly organized fiber architectures having micron-scale resolution, uniquely able to confer outstanding mechanical properties to low-stiffness hydrogels. To accomplish this, tubular MEW scaffolds were first fabricated from poly-ε-caprolactone (PCL) and incorporated into a volumetric printing vial, which in turn was exposed to the tomographic light projections required to form a 3D object in tens of seconds (**Figure 1A**). As platforms to investigate the converged technique, termed VolMEW for simplicity of reference, materials widely used in the field of biofabrication for both technologies were employed in this study: PCL for MEW, given its previously established superior printing properties and medical grade nature,^[21] and gelatin methacryloyl (gelMA) as a bioresin for VP, which has been shown to be a fast, high-resolution choice for this printing approach.^[14,33] PCL itself, as a bulk material, features an in vivo degradation time of 1–2 years, depending on molecular weight, chemical modifications, and shape into which it has been processed.^[34] Thereby, the degradation kinetics is highly dependent on the exact type of sourced material and on the morphology of the scaffold. Previous work has shown residues of FDM-processed PCL in an equine model up to 6 months after implantation within a cement blend.^[35] For MEW, due to the thin fiber diameter and relatively high surface-to-volume ratio, the degradation kinetics will be quicker, although the exact degradation time will depend also on the anatomical location in which the biomaterial is implanted. Within the articular joint of a horse model, remnants of MEW meshes were clearly seen even after 6 months of implantation,^[36] while in the periodontal region in a mouse model, histological evidence of persisting MEW fibers was detected at 6 weeks of implantation.^[37] While there is evidence showing MEW scaffolds are stable over long in vivo implantation times, consistent data elucidating in detail their degradation kinetics is currently lacking in the literature, and future research would be needed, for example, before applying these materials as vascular grafts. In the present study, different MEW mesh

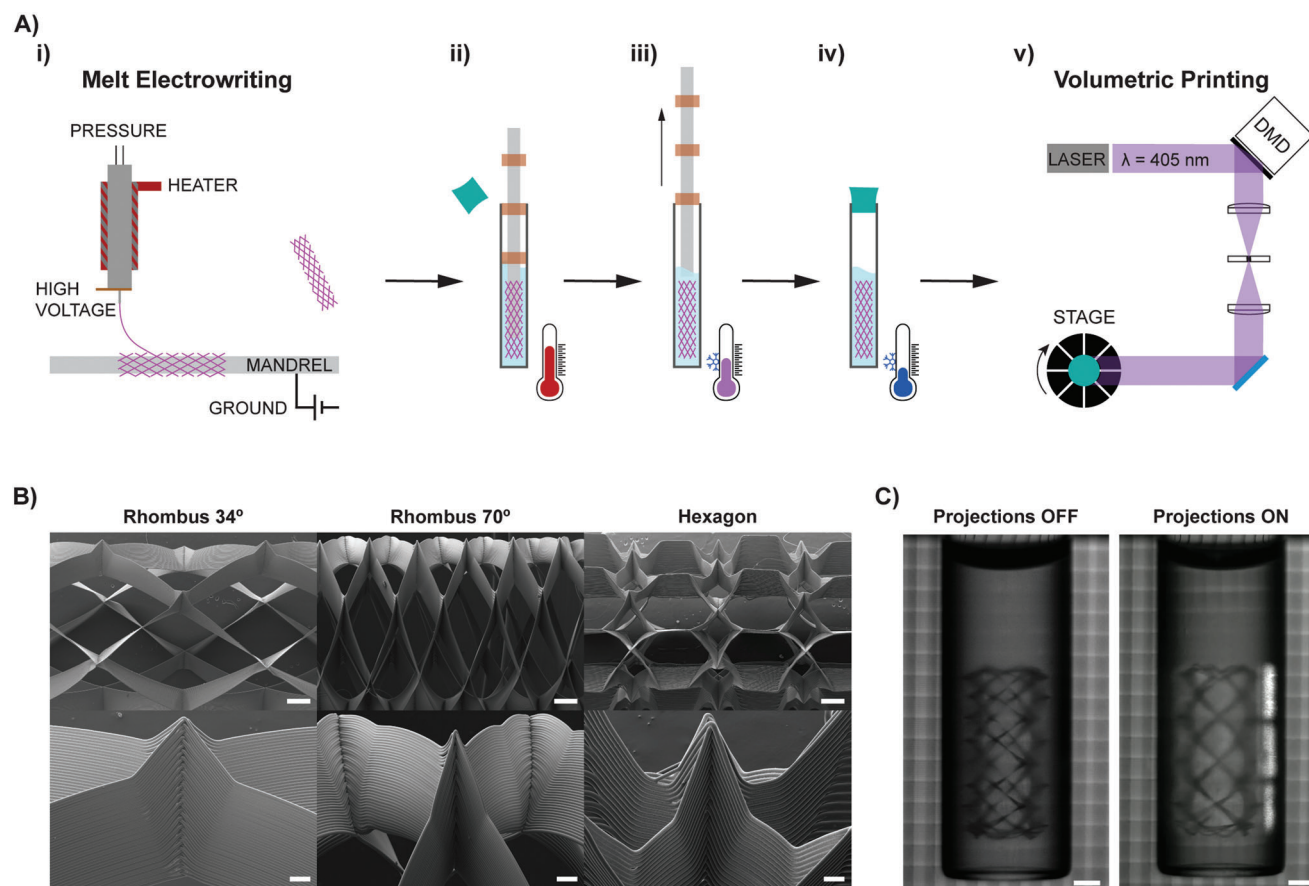


Figure 1. Convergence of MEW and VP processes—VolMEW. A) Graphical overview of: i) the fabrication of tubular melt electrowritten scaffolds on a rod and ii) their subsequent incorporation into the volumetric printing process by first placing the MEW meshes in a vial of preheated gelatin methacryloyl solution using a carbon fiber rod with centering guides. iii) Once the MEW tube is completely infused, the gelMA solution is gradually cooled as the mandrel is retracted without disrupting the gelling resin or the MEW mesh structure; iv) the vial is then fully gelled in ice water, and v) placed in the volumetric printer. The same process can be applied in the presence of cells, therefore performing a volumetric bioprinting (VBP) step. B) SEM images of three different pore structures of the tested MEW tubes (scale bars = 500 (top panels) and 100 μm (bottom panels)). C) Digital images of the volumetric printing vials containing gelMA and a fixed, centered MEW mesh when inserted into the printer and when light projections are initiated. Scale bar = 2 mm.

architectures were successfully fabricated with custom-designed pore shapes (i.e., rhombic with 34° and 70° winding angles and hexagonal (Figure 1A(i),B(ii))) and thicknesses (i.e., 20, 30, 40, and 60 printed layers). These tubular scaffolds were first placed into volumetric printer vials and guided in through a carbon fiber rod with controlled alignment (Figure S1, Supporting Information). Subsequently, the vials were loaded with gelMA. Due to the thermal gelation behavior characteristic of gelMA, the MEW mesh could be secured into its intended location and alignment even after the removal of the support rod (Figure 1A(ii)–(iv)). With the MEW scaffold aligned within the printing vial, the VP process was conducted (Figure 1A(v),C, Video S1, Supporting Information).

After establishing a simple and consistent method for setting up a hybrid VolMEW process, the effect of the opaque PCL meshes on the tomographic illumination imparted by VP was investigated to ensure the achievement of high-resolution prints (Figure 2). It was essential to first characterize this effect because the VP process relies on the undisturbed passage of tomographic

light projections through the entire bioresin vat in order to induce specific photo-crosslinking in the target regions. The presence of elements that attenuate or refract the light beams incoming from the spatial light modulator could therefore impair printing resolution. While the presence of scattering elements (i.e., cells, particles) can be mitigated by mixing the bioresin with refractive index matching compounds,^[33] the effect of opaque structures had yet to be investigated. Previous research has demonstrated the possibility to perform volumetric prints around non-transparent objects, such as metallic rods. However, such prints were only achieved with bulky structures fully encasing the abovementioned rod and lacking the fine features characteristic of volumetrically printed objects.^[38] In this study, the opacity of the PCL mesh provided a light attenuation effect by partially blocking the projection path in the regions where the PCL meshes align with the beam (occlusion points).

A custom-made setup to evaluate the light attenuation effect was devised. A laser (520 nm) was used to project a small pixel matrix through the center of a rotating VP vial containing the

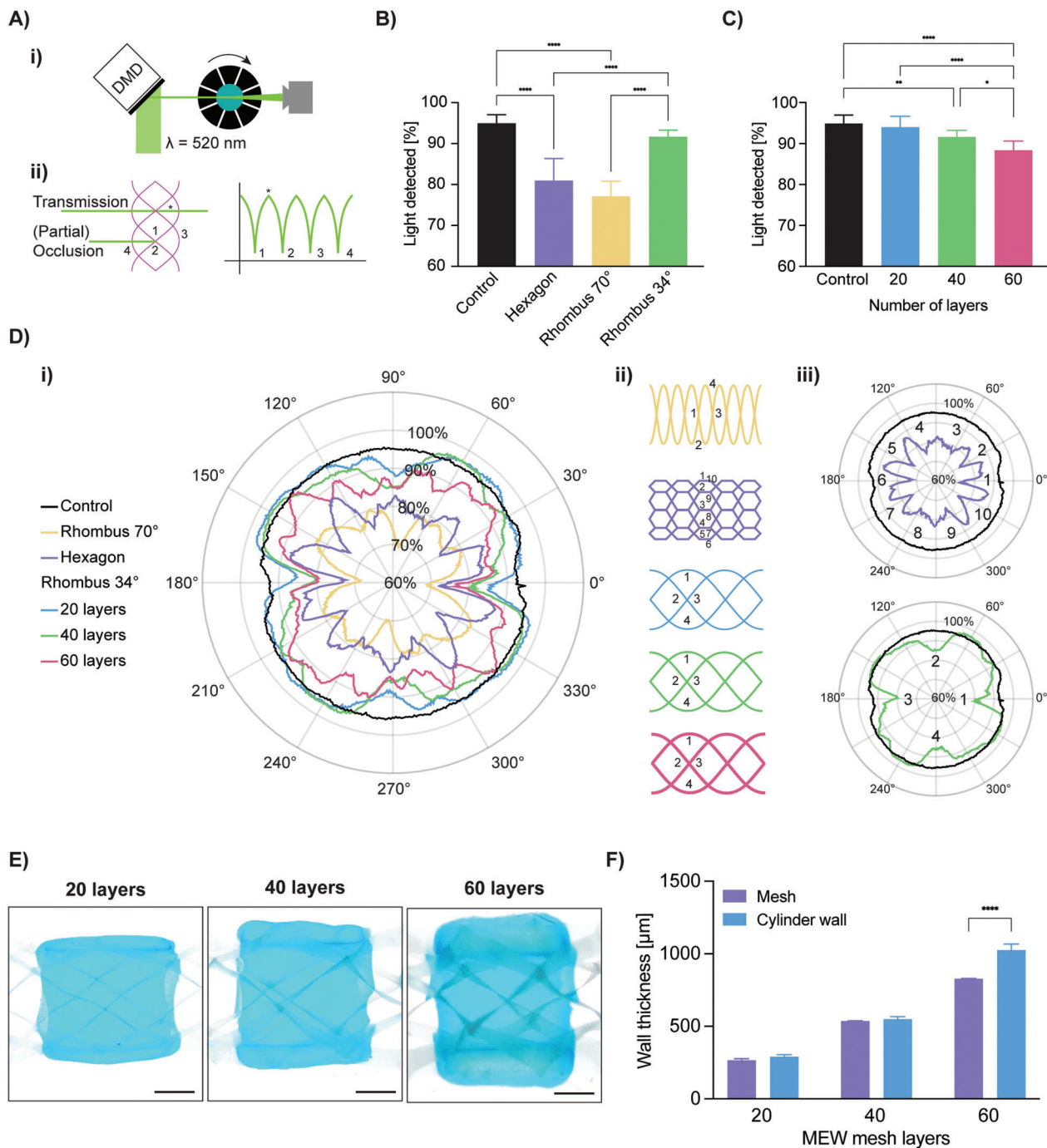


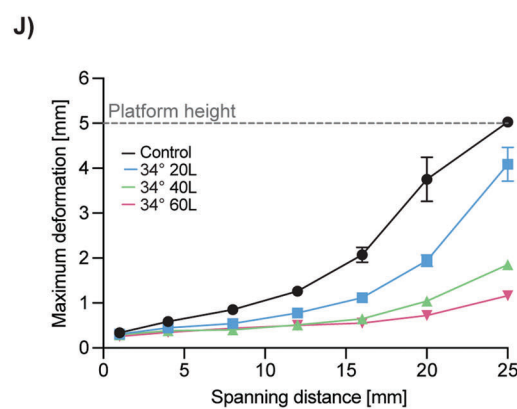
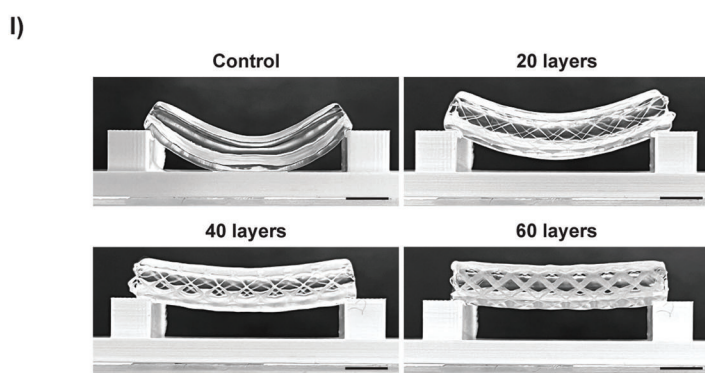
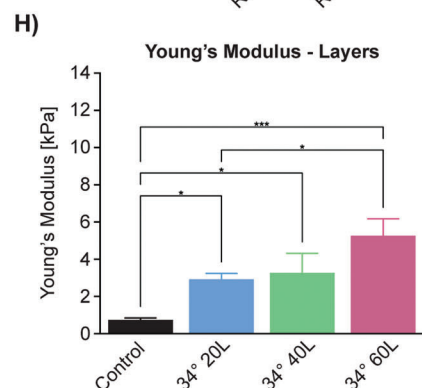
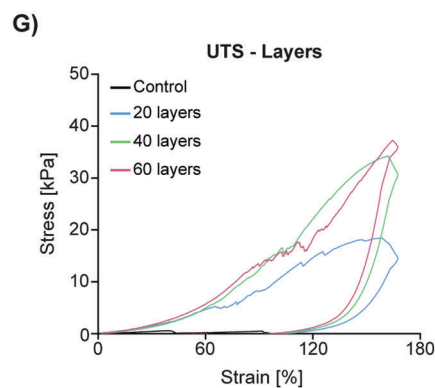
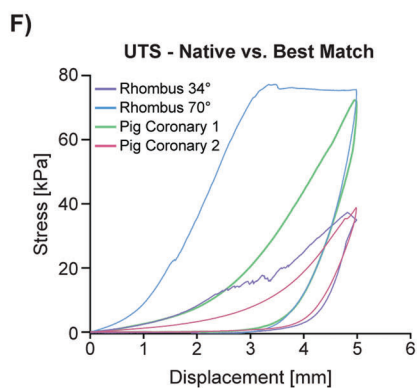
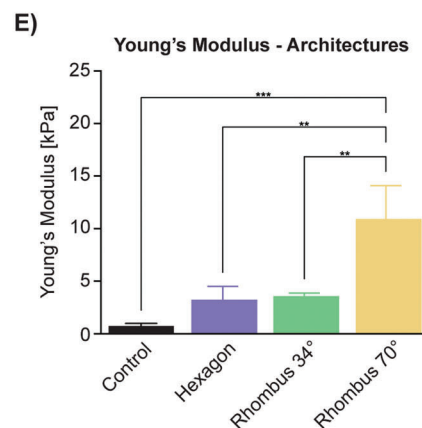
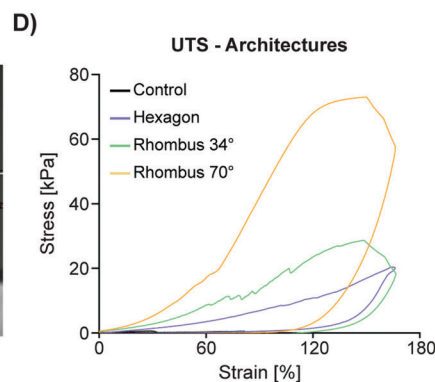
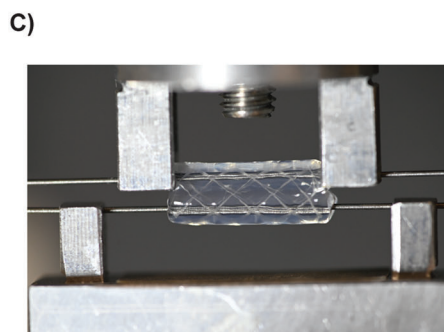
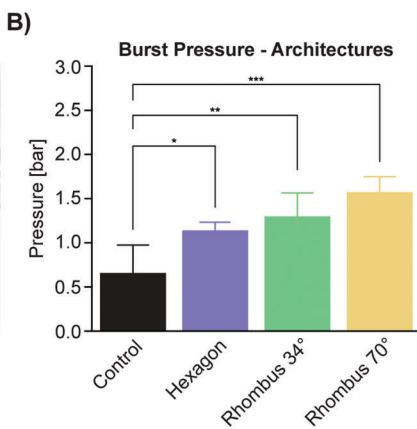
Figure 2. Characterization of the effect of MEW tube incorporation on beam path homogeneity through gelMA-filled VP vials. A) Graphical overview of the test setup used to evaluate the light attenuation effect of different architectures/layers of MEW meshes. i) A 520 nm laser beam is used to project a pixel array through a VP vial containing gelatin and different MEW tube structures for one 360° rotation while a detector placed at the opposite end of the vial captures the percentage of light passing through the vial at each angle of rotation. ii) Diagram of the numbered occlusion locations in a 34° rhombus, where the highest light attenuation is observed with an example transmission point (*) and a corresponding graph. Based on the resulting light detection measurements per structure showing the percentage of light passing through the vial, the area under the curve is plotted for B) different mesh architectures: hexagons, rhombi with 70° and 34° winding angle and mesh-free controls, as well as for C) the 34° winding angle rhombus with different number of layers (20, 40, and 60). D) i) Time synchronous average percentage of light detected for the different mesh architectures and layer heights: hexagons (40 layers), rhombi with 70° (40 layers) and 34° (20, 40, and 60 layers) winding angles and mesh-free controls ($n = 4$). ii) Architectural mesh diagrams and their respective occlusion points. Each occlusion mesh point (represented by the troughs in the graph) is numbered and iii) examples are given for the corresponding graphs. E) Stereomicroscopy images of VP-printed tubes accurately encapsulating tubular MEW meshes of 20, 40, and 60 layers respectively (scale bars = 1 mm). F) Average wall thickness of the MEW meshes with different number of layers (20, 40, and 60) and the average wall thickness of the printed hydrogel surrounding these structures ($n = 3$, scale bars = 1 mm). * $p < 0.05$, ** $p < 0.01$, **** $p < 0.0001$.

constructs with varying MEW pore architectures, or constructs with the same mesh geometry, but different layer heights. A photodetector was then placed on the opposite side of the vial, to determine the profile of the light beam passing through the hydrogel-soaked MEW mesh (Figure 2A, Figure S2, Supporting Information). The percentage of projected light intensity passing through each angle of the vial was calculated by integrating the normalized signal over a full rotation and represents the average percentage of light detected with MEW scaffold attenuations of different pore architectures (Figure 2B) and layer heights (Figure 2C). Compared to hydrogel-only control conditions, where $94.9 \pm 2.0\%$ of light intensity could be detected after passing through the bioresin vial, all three MEW pore architectures: hexagons ($80.9 \pm 5.3\%$) and rhombi with 70° ($77.1 \pm 3.7\%$) and 34° ($91.6 \pm 1.6\%$) winding angles, showed significantly lower percentages of detected light. As for the differences between architectures, the 34° rhomboid-shaped pore architecture showed the lowest attenuation effect, allowing significantly higher amounts of light passage compared to the hexagons and the 70° rhomboid. In the presence of highly opaque fiber assemblies, such as the case of our MEW meshes, light travelling through the vial is primarily attenuated by the fibers, rather than scattered. Notably, precise printing has been demonstrated previously in the presence of opaque occlusions, as, given that the light source has at least any 180° unobstructed view of the occluding object, tomographic reconstruction remains possible.^[38] The light detection plots (Figure 2D(i), Figure S3, Supporting Information) clearly visualize that the different architectures exhibit a series of steep dips where the light is partially blocked by each occlusion point (Figure 2D(ii)). Although the occlusion points coincide with a high local light attenuation, the average light passing through the vial is observed to be correlated with the pore size of the scaffold rather than the amount of total occlusion points per revolution. This hypothesis is supported by the significant difference in total percent transmitted light between 34° and 70° , where both have only four occlusion points per revolution, but the 34° rhomboid (8 pivot points) has a pore size of 4.12 mm^2 , whereas the 70° rhomboid (8 pivot points) has a pore size of only 1.01 mm^2 .^[25] Using the same setup, 34° rhombi were selected to investigate the effect of layer height based on the observed least significant light attenuation for this architecture. Here, compared to the mesh-free control, the 20-layer scaffold ($94.0 \pm 2.7\%$) did not significantly decrease the amount of transmitted light, as opposed to what was found for the 40- ($91.6 \pm 1.6\%$) and 60- ($88.4 \pm 2.2\%$) layer structures (Figure 2C). Overall, it should be noted that all these light attenuation profiles are compatible with the light transmission requirements identified in previous works, when performing volumetric printing using gelMA and LAP as resin components ($>37\%$ of transmitted light across the vial).^[14] The observed differences in light attenuation are likely caused by i) the increase in total electrowritten material, combined with ii) minor stacking errors over the entire layer height resulting in a larger occlusion zone. In addition, inherent to MEW on a rotating mandrel, each deposited layer could suffer from a minute layer shift, effectively creating a sloped and, therefore, thicker wall. Consequently, as this thicker wall rotates out of the field of view of the projected spot, it partly overcasts the detected light over a longer angular distance when compared to thinner PCL walls (Figure S4, Supporting Information).

Having shown that the degree of light attenuation can be controlled by pore architecture and layer height selection, the effect of shading on VP printing accuracy was assessed using 34° rhombic tubes at the different layer heights tested above. As a benchmark assay, we volumetrically printed cylinders with arbitrarily designed wall sizes to match the thickness of the MEW mesh ($t_{\text{print}} = 14.8 \text{ s}$). All three MEW-mesh wall thicknesses (20, 40, and 60 layers) were completely encapsulated within VP-printed gelMA cylinders of equal programmed thickness as the MEW scaffolds (Figure 2E). The thickness of the wall enveloping the 20- and 40-layer scaffolds (291 ± 13 and $550 \pm 16 \mu\text{m}$, respectively) did not significantly differ from their respective target designs (MEW mesh thicknesses) (267 ± 10 and $537 \pm 1 \mu\text{m}$ for the 20- and 40-layer meshes, respectively), suggesting that the potential effect of light attenuation for these scaffolds can be easily avoided with the selected volumetric printing light dose settings (Figure 2F). However, this was not observed for the 60-layer scaffold, where the resulting wall thickness encapsulating this structure ($1026 \pm 41 \mu\text{m}$) was significantly larger than the mesh itself ($828 \pm 3 \mu\text{m}$) (Figure 2F). The significant decrease in printing accuracy is underpinned by the light attenuation observations described previously, as this scaffold had the most noticeable effect on the passage of light through the VP sample. It is hypothesized that the thicker scaffold experiences a higher sum of diffuse backscatter reflected from the opaque PCL fibers, resulting in lower precision in delivering the light dose along the projected pattern. Consequently, off-target regions of the bioink adjacent to the MEW mesh also reached the photopolymerization threshold. Despite this effect seen in the thicker MEW samples, it is noteworthy that all three mesh thicknesses allowed VP to occur and produced homogeneous cylindrical prints. Moreover, if thicker MEW scaffolds are required for specific applications, this information on the light attenuation profile could feed future algorithms to computationally correct the tomographic projections.

In previous research focused on the VP technique for bioprinting applications, biocompatible bioresins obtained from hydrogel-based materials with relatively low mechanical stability have been used. On the one hand, these classes of hydrogels are desirable when it comes to maintaining cell viability and facilitating cell-to-cell communication.^[14,33,39,40] On the other hand, these bioresins are often not strong enough to withstand the harsh mechanical environment found in native tissues, be it shear, tensile, or compressive forces. The VolMEW approach has the potential to overcome this challenge and enhance the mechanical stability of the printed structures, enabling a range of tissue-specific load-bearing applications in line with the mechanical stabilization that has been achieved when MEW was combined with extrusion-based bioprinting.^[32,41] To determine the mechanical properties of the hybrid VolMEW constructs, the burst and tensile performance of the composite prints were tested.

First, the burst pressure of the tubes was assessed by connecting the VolMEW tubes to a custom-made test setup via microfluidics adapters and commercially available tubing (Figure 3A, Figure S5A, Supporting Information). Different from what was experienced with reinforced tubes, simply mounting constructs made from non-reinforced gelMA to the adapters was difficult, as these prints tended to rupture while being secured in place (Video S2, Supporting Information). Vaseline was injected into the luminal cavity of the tubes and the pressure was recorded



until failure (Video S3, Supporting Information). A significant difference in burst pressure was recorded for the different geometries, which displayed increased strength when compared to the gelMA-only controls (Control: 0.66 ± 0.32 bar/Hexagon: $1.14 \text{ bar} \pm 0.10 \text{ bar}/34^\circ$: $1.3 \pm 0.26 \text{ bar}/70^\circ$: $1.58 \pm 0.17 \text{ bar}$) (Figure 3B). Overall, these results corroborate previous observations of hydrogel-infused tubular MEW scaffolds, which also showed enhanced tensile properties and resistance to flow-based pressures. Nevertheless, it should be noted that, in terms of absolute values, our results differ from previous burst pressure evaluations that have been done with heterotypic tubular graft systems as a balloon catheter has been used to inflate the construct.^[31] To better capture the flow dynamics of a liquid exerting the pressure onto the lumen of the construct, and prevent drying out of the hydrogel, we opted for vaseline as a conductor for its incompressibility that would allow to exert the applied air pressure onto the construct and thus offer a form of comparison towards other comparable experimental setups with pressurized air. Vaseline also made it easier to notice small, damaged areas, as it formed ribbon-like shapes, which could be easily evaluated as failure of the construct (Figure S5B, Supporting Information). From a physiological perspective, the measured values are above the maximum arterial pressure, but below expected burst strength recordings for native vascular systems.^[42] Nevertheless, the measurements reveal the possibility of modifying these parameters by adapting the reinforcement geometry of the hybrid construct and adjusting the properties of the hydrogel via its composition. Moreover, it should be noted that, in a tissue engineering application, cells could be added to the printed scaffold prior to implantation, and the constructs could be subjected to an in vitro maturation step to finally match the desired mechanical properties for in vivo utilization.^[43]

Next, a custom two-pin setup was mounted on a uniaxial tensile testing machine capable of cyclic motion and samples were mounted by inserting the pins through the lumen of the construct to perform radial tensile tests (Figure 3C). In this fashion, a motion similar to the dilation of blood vessels during systole could be replicated and recorded. This is a relevant parameter to quantify, because the compliance of a tubular construct is associated with the likelihood of graft occlusion and ultimately rejection, especially for small-diameter vascular structures.^[44] Another advantage of testing circular constructs in radial tensile experiments is that it more closely approximates physiological mechanical properties compared to the planar axial method of cutting the tube longitudinally and clamping it onto the testing machine.^[45] Conversion to stress and strain values were calcu-

lated using formulas previously used in wire myography.^[46] In order to evaluate the tensile performance of the composite materials, samples were strained to 5 mm, which equates to 166% elongation, a value chosen as a reference point as it exceeds physiological vascular strain levels. Figure 3D illustrates the behavior of VolMEW constructs with different reinforcement geometries compared to unreinforced constructs. Each of the reinforcement geometries showed a different hysteresis curve over cyclic loading, and all of them allowed the VolMEW constructs to withstand a full cycle of stress loading, which instead resulted in failure for VP-only (gelMA-only) constructs. A significant overall increase was shown in the recorded peak stress values for all reinforcement strategies, with hexagonal pores (20.3 ± 3.2 kPa), rhombic pores with 34° (28.7 ± 4.9 kPa) and 70° (73.0 ± 21.5 kPa) winding angles, outperforming gelMA-only controls (5.2 ± 2.1 kPa). Overall, the strongest reinforcement in terms of Young's modulus was provided by the 70° rhombic structure (10.8 ± 3.3 kPa) when compared to 34° rhombic (3.5 ± 0.3 kPa) and hexagonal (3.2 ± 1.2 kPa) structures (Figure 3E). The difference is likely caused by the specific pore sizes present in these MEW constructs as well as the compliance of the different repeating compartments in deforming along with the hydrogel during the tensile displacement. The effect of pore size of MEW meshes has already been characterized in previous studies.^[25,47] The hexagonal constructs feature a higher stiffness compared to the rhomboid structures in radial deformation as an effect of their geometry, which is likely the main cause for the linear rise of stress in the recorded measurements and is supported by other studies on the influence of MEW geometries on their mechanical behavior.^[48] The rhomboid structures illustrated a certain degree of flexibility depending on the winding angle, allowing the construct to behave elastically in the direction of radial tensile deformation before transitioning to plastic deformation. This allows the rhomboid geometry to assume vastly different mechanical properties depending on the chosen winding angle.^[49] The aforementioned effect is presented in the recorded difference between the 34° (Peak Stress 28.7 ± 4.9 kPa/Young's modulus 3.5 ± 0.3 kPa) and 70° (Peak Stress 73.0 ± 21.5 kPa/Young's modulus 10.8 ± 3.3 kPa) rhomboid orientations (Figure 3D). The deviation between the generated samples is minimal within their group (apart from the 70° rhomboid constructs), highlighting the stable manufacturing process of the VolMEW constructs. The hexagonal structures differ from the rhomboids in their elastic properties due to the higher number of crossover points and the overall stable hexagonal geometry, resulting in a nearly linear mechanical behavior over the entire displacement range. For biological

Figure 3. Mechanical properties of VolMEW constructs with different mesh architectures and number of layers. A) Photograph of the burst pressure test setup with the construct mounted and pressurized using part of a custom 3D printed bioreactor assembly. B) Burst pressure evaluation between different MEW reinforcement geometries (30 layers). C) Photograph of the customized mounting setup on the uniaxial tensile testing machine with the VolMEW construct in place. D) Ultimate tensile stress analysis for architectural differences between the tested MEW geometries (30 layers) within the VP tubes. Constructs were displaced to 5 mm, corresponding to 166% strain. E) Graphical depiction of Young's moduli compared between MEW geometries (30 layers). F) Comparison of VolMEW construct UTS measurements with porcine coronary artery measurements obtained using the same tensile test setup and parameters. G) Ultimate tensile stress analysis of different layers of MEW construct reinforcement. H) Graphical representation of Young's moduli compared between different layers of MEW construct (34° rhombus geometry). I) Bending resistance was assessed by placing a volumetrically printed gelMA tube reinforced with 34° winding angle rhombus MEW meshes of different number of layers (0, 20, 40, and 60) on two 5 mm-tall columns spanning 25 mm in length to evaluate the maximum deformation of the printed construct (scale bars = 5 mm). J) Plotted average maximum deformation of control samples without MEW reinforcement and tubes reinforced with 34° winding angle rhombus MEW meshes of different number of layers (0, 20, 40, and 60; dotted line represents the maximum height of the columns on which the constructs were placed). * $p < 0.05$, ** $p < 0.01$, *** $p < 0.001$. $n = 3$ for mean values, unless indicated otherwise.

applications, connective tissues and blood vessel walls are typically characterized by tensile stress–strain curves with an initial toe region (Figure S6, Supporting Information), indicative of the gradual recruitment of the ECM fibers in the direction of the application of the stress, followed by a stiffer region at higher deformations. A similar profile can be obtained with the rhombic MEW reinforcements at low winding angles (34°), while stiffer meshes in the radial direction can be obtained at higher winding angles (70°).^[49] To enable a comparison to natural tissues, two porcine coronary arteries were measured in the same fashion as the VolMEW constructs. When comparing the rhomboid constructs to the porcine coronary arteries, the 70° (Blood Vessel 1: 72.4 kPa/70°: 75.5 kPa) and 34° (Blood Vessel 2: 38.7 kPa/34°: 37.3 kPa) VolMEW constructs showed a good approximation of the maximum stress levels, while the 34° rhomboid reinforced constructs also showed a comparable overall curve trajectory to the physiological specimens (Figure 3F). Due to interpatient variability and the wide range of mechanical properties that vessels display even when taken from adjacent anatomical locations,^[50] these results underscore the versatility of the proposed VolMEW system to modulate the mechanical profile of the printed composite tubes in order to approximate physiological blood vessel mechanics and to utilize the mesh design to account for natural variation. In summary, the presence of the MEW scaffolds endows the otherwise mechanically weak hydrogel construct with superior mechanical properties, and stress–deformation profiles approaching those displayed by native vessels.

Based on these findings, combined with the previously established superior light attenuation performance, further experimentation focused on the 34° rhombus geometry. A major benefit of MEW is the highly organized manner of fabrication and the consistent stacking of fibers, enabling a high degree of reproducibility and an additional adjustment point for mechanical properties.^[51,52] The evaluation of the effect of different layer heights for the 34° rhomboid constructs illustrated an increase of maximum recorded stress (20L: 18.5 ± 4.2 kPa/40L: 34.3 ± 3.3 kPa/60L: 37.3 ± 1.5 kPa), as well as an increase of Young's modulus. (20L: 2.9 ± 0.3 kPa/40L: 3.3 ± 1.1 kPa/60L: 5.3 ± 0.9 kPa) (Figure 3G,H). Assessing the ability of the constructs to operate in a range of strains closer to biological values over an extended period is a valuable metric to record when looking into the mechanical properties of tubular constructs. A 200-cycle displacement to 20% strain was used, and it revealed an increase in stiffness as a function of the number of layers of the MEW reinforcement geometries (control: 1 ± 0.3 kPa/20L: 3.6 ± 0.2 kPa/40L: 3.8 ± 1 kPa/60L: 6.0 ± 1.3 kPa), except for the difference between 20 and 40 layers, where the SD and limit of recording resolution prevented any discernible significance from being recorded (Figure S6C, Supporting Information). It should be noted that although we focused on PCL as the MEW platform material and gelMA as VBP material in this study, the mechanical properties of the MEW fiber reinforcements could also be tuned by utilizing different biomaterial inks.^[53–55] Regardless of the choice of material used for the fibrous reinforcement, another aspect to keep in mind in composite materials is the strength of adhesion between the fibrous inclusions and the embedding matrix (the hydrogel). In our case, observing the fracture behavior of the composite materials under tensile testing, it is possible to

appreciate how failure occurs predominantly within the GelMA component, with the formation of a crack longitudinal to the direction of the bar used to apply the mechanical stress (Figure S7, Supporting Information). Notably, the fracture does not occur at the interface between the GelMA and the PCL fibers, nor is it aligned with the fibers themselves. This suggests that the interfacial strength between the two materials is likely superior to the tensile strength of the GelMA itself. Despite this, should it be necessary for future applications to further improve the hydrogel–MEW mesh adhesion, several strategies have been reported in the literature, including surface treatments to the PCL to improve hydrophilicity,^[23] or the introduction of covalent bonding between the two components,^[56] among other possibilities.

In addition to tensile testing and burst pressure analyses, the shape stability of these VolMEW cylinders was assessed by evaluating their bending resistance. While a degree of bending flexibility can be desirable to manipulate the VolMEW tubes, unwanted collapse due to the inability of the tubes to sustain their own weight can be detrimental. The experiment was set up in a manner similar to the previously proposed filament collapse test, which has been used to evaluate the filament stability of extrusion-based printing materials.^[57] Briefly, long (27.5 mm) composite tubes ($t_{\text{print}} = 16.4$ s) were placed to bridge the distance across two columns spaced at increasing distances from each other (1–25 mm), and the gravity-induced flexural deformation of the tube was imaged and measured, as a function of the layer height (34° rhombic geometry) (Figure 3I,J). The most striking effect of the reinforcing MEW scaffolds was observed at the longest spanning distance of 25 mm. At this gap distance, where meshless 8% (w/v) gelMA cylinders completely collapse over the entire height of the column structure, increased resistance to bending is observed in the hybrid VolMEW samples as layer height increases (Figure 3I, Figure S8, Supporting Information). Spanning the largest gap of 25 mm, the 60-layer construct only underwent an average maximum deformation distance of 1.16 ± 0.04 mm, significantly less than the 40- and 20-layer constructs (1.85 ± 0.05 and 4.09 ± 0.38 mm respectively). A similar trend in bending resistance was also observed for some of the smaller spanning distances (20, 16, and 12 mm), down to the 8 mm gap and below, where the maximum deformation becomes undetectable across all samples (Figure 3J). Importantly for the versatility of this approach, it was also demonstrated that lower gelMA concentrations (e.g., 5% w/v), which are often necessary for different cell types to thrive, the reinforcing effect of the MEW meshes is still evident in this bridging test (Figures S9 and S10, Supporting Information). Overall, these mechanical evaluations confirm that the convergence of MEW with VP results in hybrid constructs exhibiting superior mechanical stability compared to gelMA-only constructs, thus enabling applications of these hydrogel-based constructs in a broader array of biologically relevant settings.

With a thorough understanding of the mechanical reinforcement provided by MEW fibers in the established VolMEW converged approach, the unique advantages of the VP process were further explored to create advanced and geometrically complex tubular structures (Figure 4). Attempting to introduce cell-laden hydrogels within tubular porous structures, such as those produced by fused deposition modeling, MEW, or solution electrospinning could be simply performed via casting in tubular molds. A major drawback of such casting approaches is the lack of pre-

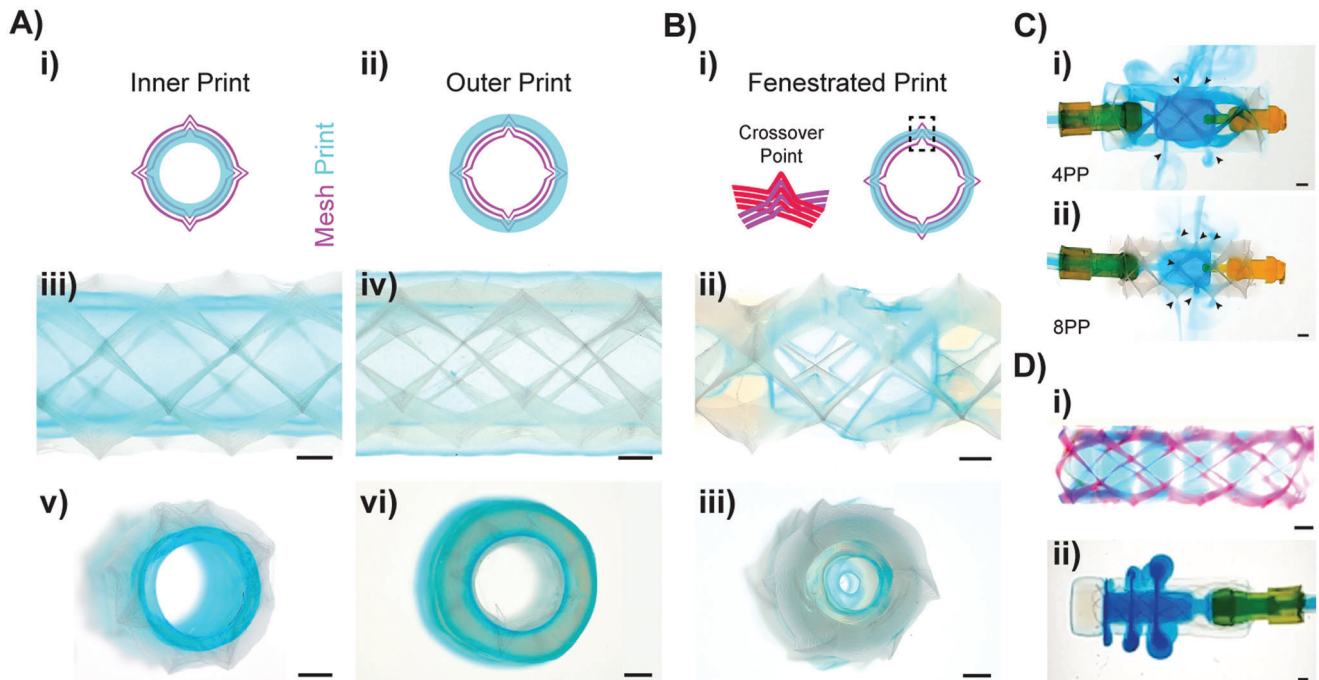


Figure 4. Printing of complex tubular structures and fenestrations. A) Graphical overview of possible inner (i) and outer (ii) printing strategies, in which the hydrogel embeds only the inner or outer region of the MEW construct respectively, leaving the rest exposed. Stereomicroscopic images of these inner (iii,v) and outer (iv,vi) prints from top (iii,iv) and side (v,vi) views. B) VolMEW printing of fenestrated tubular constructs. i) Graphical representation of the characteristic crossover points of tubular MEW meshes, and the resulting fenestrations when a thin layer of bioresin is printed exactly in the middle of the MEW construct. Stereomicroscopic images of the top (ii) and side (iii) views of such fenestrated structures. C) MEW-induced fenestration showing local filtration at crossover points where the mesh pierces the hydrogel construct with adjustable leakage over time (i,ii) based on the number of crossover points (black arrows) controlled by pivot points (PP). D) Circular fenestrations: i) Lightsheet maximum projection highlighting the ability to tailor fenestration size. ii) Light microscopy image of the perfusable VolMEW construct with controlled leakage of Alcian Blue stain through the fenestrations, undisturbed by the presence of the MEW meshes. Scale bars = 1 mm.

cise control, which only allows the production of homogeneous cylindrical tubes consisting of a single gel layer (and thus a single layer of encapsulated cells). Alternative approaches are therefore needed to obtain, for instance, multilayered walls analogous to those found *in vivo* in vessels larger than 100 μm in diameter. With the positional accuracy provided by VP, the relative orientation of the hydrogel layers in relation to the MEW mesh can be freely designed and modified (Figure 4A). This was demonstrated with prints in which the hydrogel layer reached the center of the mesh, leaving either the outer region of the scaffold gel-free (inner print; Figure 4A(i),(iii),(v)) or its inner region gel-free (outer print; Figure 4A(ii),(iv),(vi)). Such structures would have potential applications in vascular tissue engineering by allowing a second layer of gel to be printed over the exposed region of the scaffold to guide cell attachment and directionality,^[28,58] or to incorporate multiple materials and cell types within the same construct. Another physiologically relevant application of the positional control of hydrogel printing within the MEW mesh is the creation of micron-scale fenestrations (Figure 4B), features resembling, albeit at a larger scale than native structures, those commonly found in permeable vessels throughout the human body. These fenestrated vessel walls, already present in neovascular structures during development,^[59] are abundant in different regions of the body where permeability is critical for nutrient and waste exchange, including the renal glomerulus,^[60] intestinal blood vessels,^[61] the nasal mucosa,^[62] and are present in different

areas of the central nervous system,^[63] including the blood-brain barrier in certain neurological diseases including strokes.^[64–66] Apart from these naturally occurring fenestrated structures, the clinical application of fenestrated stents for the repair of damaged vessels and aneurysms has also been a topic of interest, given the need to maintain transmembrane transport in the repaired vascular structures.^[67–69] In this study, we have demonstrated how to generate similar types of leakage points throughout VolMEW printed tubes by taking advantage of the natural interactions at the interface between the bioprinted hydrogel structures and the MEW mesh (Figure 4C). During the fabrication of MEW scaffolds, intersecting print paths of the same layer (crossover points) create a local elevation due to more material being stacked on top of each other, while at the same time, there is a sagging effect between two crossover points that further amplifies the elevation effect. These crossover points are herein exploited to create fenestrated structures (Figure 4C(i)). To achieve this, hollow gelMA cylinders were volumetrically printed exactly in the center of a MEW scaffold, leaving the inner base of the mesh and the tip of the crossover points exposed, allowing for small fenestrations (≈ 10 -micron range, comparable to the MEW fiber thickness) to form on the outer surface of the hydrogel layer (Figure 4C(ii), (iii)). These small fenestrations were successfully produced throughout long tubular structures and remained perfusable, as evident by the outflow of Alcian Blue stain through the exposed crossover points (Figure 4D, Videos S5–S7, Support-

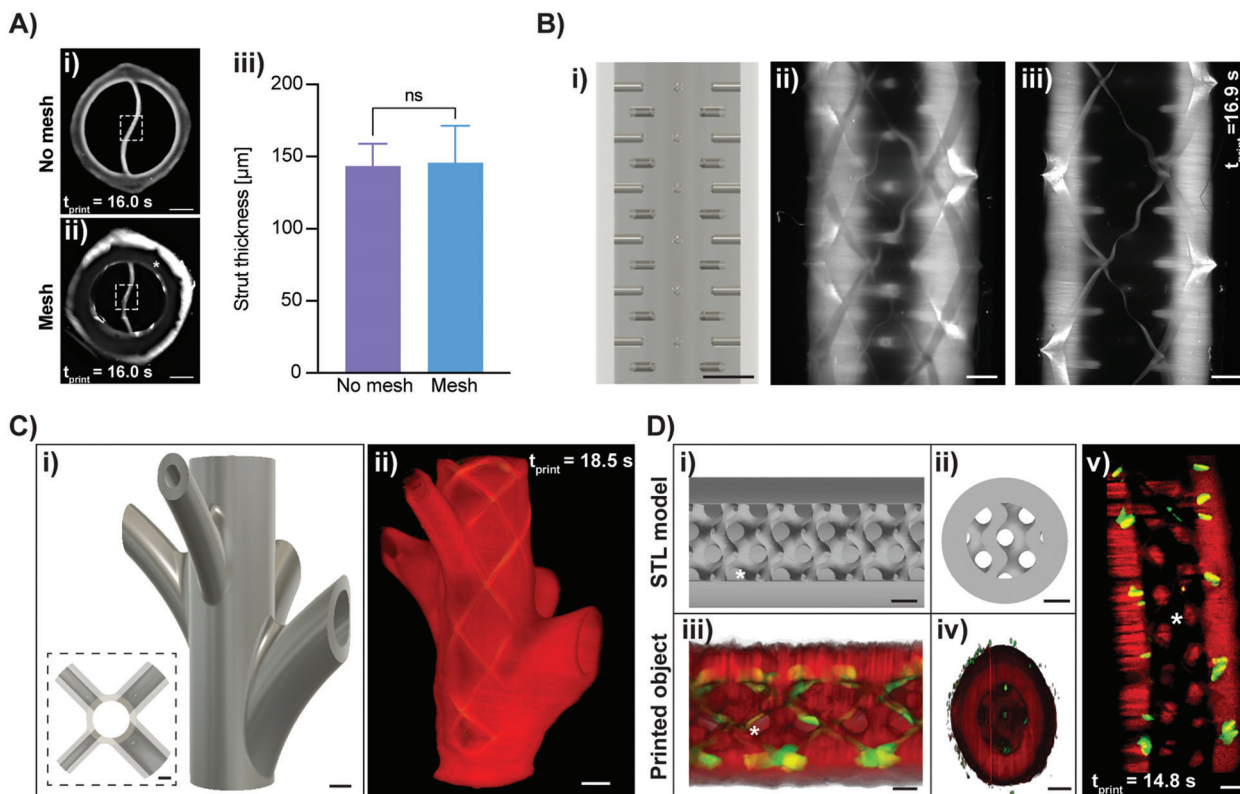


Figure 5. High-resolution VolMEW printing demonstrating external and internal features of physiological relevance. A) Printing resolution of positive features in mesh-free samples: i) as shown through stereomicroscopy images and in the presence of a 40-layer MEW mesh, ii) as shown in a lightsheet microscopy image (dotted-box represents the measured strut, asterisk represents the area in which the MEW mesh is embedded). iii) Comparison of printing resolution between mesh-free and mesh constructs ($n = 5$). B) i) Digital model of a tubular structure consisting of several interspaced villus-like structures protruding into the lumen of an open channel, and ii,iii) different lightsheet microscopy slices of the model showing the presence of villi throughout the tubular structure. C) i) Digital model of a branched structure with channels of different diameters (dotted box shows the top view of the model) and ii) 3D reconstruction of the printed structure from lightsheet microscopy imaging. D) i,ii) A digital model of a VolMEW printed Schwarz D structure inside a cylinder containing the reinforcing MEW mesh from lateral and vertical cross-sectional views and iii,iv) the corresponding lightsheet 3D volume reconstructions and v) a central lightsheet fluorescence image of the printed structure with the gel structure (red) and the encapsulated MEW mesh (green) highlighting the high printing resolution within the inner diameter of the mesh. Scale bars = 1 mm.

ing Information). Importantly, the number and distribution of these fenestrations can be controlled by adjusting the number of pivot points of the MEW tubes, an easily adjustable parameter in the code used to fabricate these tubular scaffolds. It is clearly visible that the 4-pivot point scaffold (Figure 4D(i)) yields fewer fenestration regions compared to the 8-pivot point scaffolds (Figure 4D(ii)). The VP design alone was also tested to fabricate fenestration-like structures of decreasing size by stacking cylinders on top of each other with a minimum reproducible gap size of $464 \pm 48 \mu\text{m}$ (Figure 4E(i)). These cylinders remained bound together by the interwoven MEW fibers and also allowed lateral Alcian Blue outflow (Figure 4E(ii), Video S4, Supporting Information). The combination of macroscale VP- and micrometer-scale crossover VolMEW fenestrations (as low as hundreds of nanometers)^[52] could introduce hierarchical pore distribution with spatial control along the length of the tube, while spanning a wide range of pore sizes within the same hydrogel shell. It should be noted that the density of larger, VP-induced pores should be carefully controlled, as placing too many of these gaps in close proximity to each other could significantly affect the structural stability of the printed constructs. Furthermore, it is important

to note that the resolution of these fenestrations is determined by the thickness of MEW fibers and does not match native fenestration sizes. However, this approach could be exploited for other in vitro applications that require the controlled creation of microscale pores, and further developed to more closely mimic native structure scales. These experiments further demonstrate the potential of the VolMEW convergence, as the incorporation of MEW constructs not only plays a mechanical role in VP printing, but can also be exploited to create more complex, native-like tubular structures when combined with the design freedom offered by volumetric printing.

In addition to introducing the freedom to control the degree of alignment and the presence of pores and fenestrations, the hybrid VolMEW approach also facilitates, for the first time, the integration of complex architectural structures in the outer and inner regions of the MEW-reinforced tubular structures (Figure 5). Current approaches, based on hydrogel casting and extrusion bioprinting do not easily allow for the integration of complex architectural elements around and within the pre-existing MEW mesh, mainly due to the presence of moving needles in extrusion printing, and the challenges of mold removal in the case

of casting. By fully encapsulating the MEW scaffold in a single step using the VP approach, hydrogel regions with increased design freedom were created. Importantly, it was first shown that the light attenuation effect of the MEW mesh on the VP process explored in Figure 2 did not affect the printing resolution of features within the tubular structures (Figure 5A). To do this, the differences in feature size of a sinusoidal strut running through the lumen of a VolMEW tube were evaluated in comparison to hydrogel-only prints (Figure 5A(i),(ii)). The average strut thickness between the mesh-free and reinforced constructs did not exhibit significant differences, thus further cementing the fact that the light attenuation induced by the MEW mesh did not hinder the VP process (Figure 5A(iii)). To illustrate the ability to print distinct, high-resolution components within the MEW mesh in a more widely distributed manner, a tubular structure lined with villi-like pillars oriented at different angles was successfully resolved (Figure 5B). The villi structures were successfully resolved ($232.3 \pm 35.5 \mu\text{m}$ average thickness), did not fuse to one another, and could be designed to match physiological length-to-width ratios.^[70,71] It should be noted that the purpose of these printed structures is to highlight the potential to resolve protrusions that can be easily produced within the PCL mesh-laden tubes via volumetric printing, but not with other approaches, and that native intestinal villi in humans show comparable dimensions, but are present at higher densities. Next, to demonstrate the addition of complex geometries on the outer side of the VolMEW tubes, branching channels stemming from the reinforced tube were successfully printed ($t_{\text{print}} = 18.5 \text{ s}$). Both the reinforced and non-reinforced channels were homogeneously perfused, as the porous MEW mesh allowed for a seamless connection between the channels, demonstrating the potential to create more complex and reinforced branching structures that are crucial to replicating native vascular networks (Figure 5C). Additionally, the ability to print complex structures within the lumen of VolMEW reinforced tubes was demonstrated, and a mathematically derived Schwarz D lattice was printed within the gelMA cylinder, as proof-of-concept design (Figure 5D). While these types of structures have previously been printed on a volumetric printer,^[33] it is remarkable that, even in the presence of the opaque MEW mesh, these fully perfusable structures could be resolved with a printing accuracy of $764 \pm 48 \mu\text{m}$ ($t_{\text{print}} = 14.8 \text{ s}$).

The presented range of architectures printed within reinforced VolMEW tubes highlights the fact that the inherent freedom of design of VP is maintained in this hybrid approach, and can bring about important advantages to different applications in tissue engineering. Another of these advantages was the incorporation of customizable, modular components to the tubular models shown here, that could facilitate the direct connection of VolMEW structures into leak-free perfusion systems (Figure 6). The role of perfusion in the development of native-like tissues has been thoroughly explored in the field of tissue engineering, with the development of dynamic perfusion bioreactors and microfluidic systems gaining increasing interest in the last years.^[72] Here, a major challenge when working with soft hydrogels is ensuring a tight and leak-free perfusion that can be maintained for long-term culture. In conventional casting/molding approaches, incorporating customizable inlets comprising a combination of narrowing and opening lumen diameters that allow for these tight connections is very difficult when not unfeasible, espe-

cially when using low-stiffness hydrogels like the ones applied in this work. Figure 6 demonstrates how VolMEW can leverage the design freedom offered by VP to create readily perfusable constructs by incorporating fitting inlets to the tubular prints shown throughout this manuscript. First, custom-made connectors consisting of an O-ring to seal the inlet point of the tubular structures were developed, and a negative of these structures was incorporated into the tubular structure 3D models (Figure 6A(i),(ii)). These modular constructs enabled the leak-free, sterile perfusion of simple tubular structures for up to 7 days under sterile conditions (tested in cell-free constructs), whereas the connector-free, straight tubes immediately exhibited multiple leakage points (Figure 6A(ii),(iii)). To demonstrate the feasibility and functional advantages of these modular constructs, perfusable models showing asymmetric ($t_{\text{print}} = 18.5 \text{ s}$; Figure 6B) and symmetric ($t_{\text{print}} = 16.0 \text{ s}$; Figure 6C) narrowing of the VolMEW lumen to mimic stenosis were printed and could be immediately perfused. Continuous blood perfusion (Figure 6C(iii)) through the symmetrical stenosis model resulted in a rapid blockage of flow at the stenotic region of the construct, and upon gentle flushing the formed blood clot could be observed occluding the narrow region of the construct (Figure 6C(iv)). To highlight the versatility of this modular approach, a simplified venous valve model (Figure 6D(i)) was successfully printed at high resolution within VolMEW reinforced tubes, with leaflets measuring $232 \pm 10 \mu\text{m}$ ($t_{\text{print}} = 11.9 \text{ s}$) (Figure 6D(ii)). The valve, as found in the native structure, was able to control flow in a unidirectional manner in response to flow pressure, with the leaflets bending towards each other and closing, preventing flow in one direction (Figure 6D(iii), Videos S8 and S9, Supporting Information), but remaining unstressed and open in the other direction, allowing uninterrupted flow (Figure 6D(iv)). In this case, a differently shaped connector was used, further showing the versatility of the VP, moldless- and contactless approach, to accommodate for virtually any geometry. The male part of the connector, could be produced on-demand using Digital Light Processing (DLP) printing, and tailored to the perfused structure and perfusion flow rates necessary for specific applications as previously shown.^[72]

After successfully demonstrating the ability to print these different geometric features (complex branched structures, stenosis models, valves, etc.), create ready-to-perfuse systems, and given the promising mechanical properties of the hybrid VolMEW scaffolds, the possibility of forming cell-laden constructs containing multiple cell types by both direct bioprinting and by post-print seeding was investigated. To make this possible, we devised a strategy to sequentially, and volumetrically print multiple cell-laden hydrogel layers (Figure 7A), followed by a seeding phase in the lumen of the tube, resulting in a three-layer construct (Figure 7B). As a preparatory step, using a single fluorescently labeled suspension of human mesenchymal stromal cells (DiD-hMSCs), it was shown that cell-laden gelMA resins could be printed to precisely envelop the MEW scaffold ($t_{\text{print}} = 14 \text{ s}$), and the resulting hybrid, cellularized construct maintained high cell viability (Figure S11, Supporting Information) and could then be seeded with human umbilical vein endothelial cells (HUVECs) after printing (Figure 7C). This resulted in a two-layer construct with independent cell regions, an inner HUVEC layer (Figure 7D(i)), and a 3D gelMA layer encapsulating hMSCs and the MEW scaffold to provide

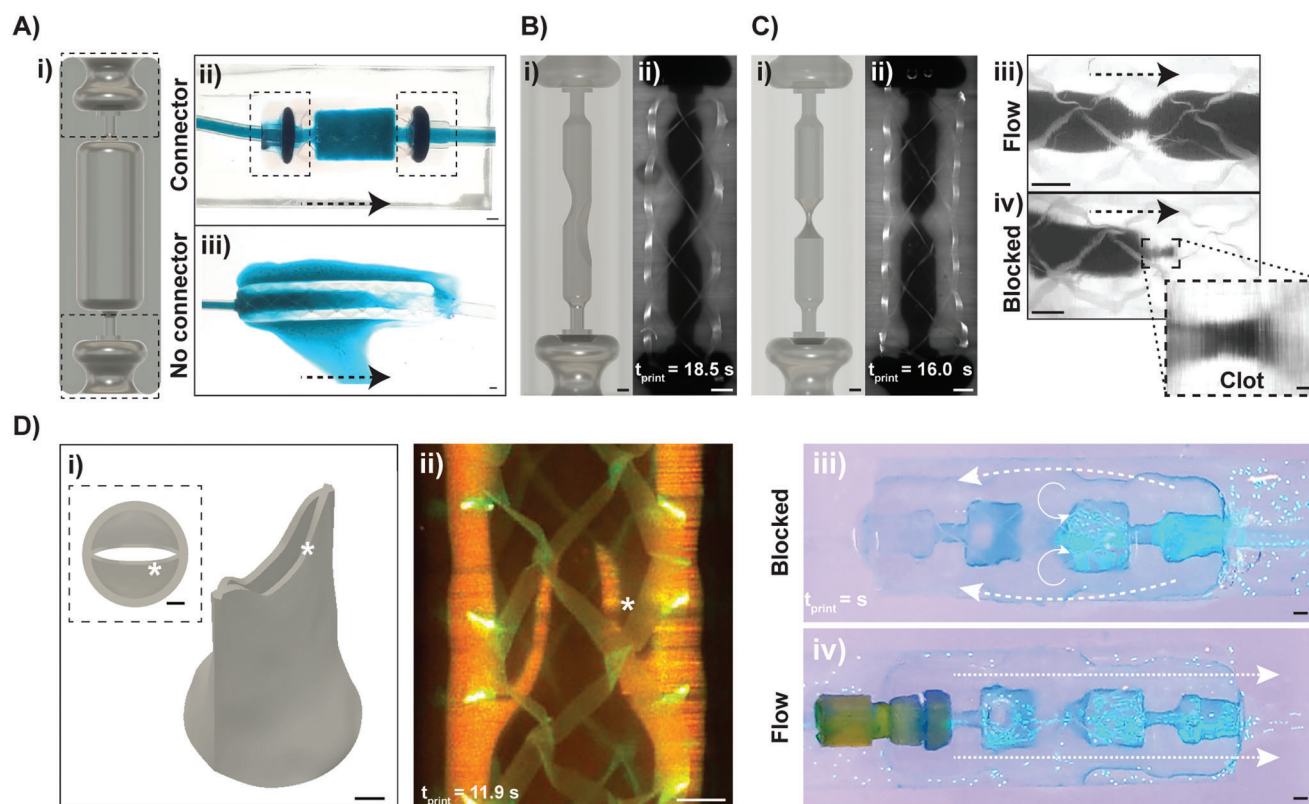


Figure 6. Volumetric printing of custom connectors to create leak-free perfusable systems of physiological relevance with flow-dependent behavior. A) i) Digital model of a custom-made connector printed as an inlet and outlet of a MEW-reinforced tubular structure (the dotted line shows the connector area added to the tubular print model). ii,iii) Stereomicroscopy images of VolMEW-printed tubes with (ii) and without (iii) the custom-made connector (dotted lines) ends as they are perfused with Alcian Blue solution to visualize leakage points (the arrows indicate the direction of flow). B) i) A digital model of a VolMEW complex stenosis model showing asymmetrical channel narrowing along the length of the printed tube and ii) a lightsheet microscopy image showing the inside of the resulting printed channel. C) i) A digital model of a VolMEW stenosis model with symmetrical narrowing of the lumen, and ii) a lightsheet microscopy image showing the inside of the resulting printed channel. iii) Constant perfusion (arrows represent the direction of flow) of blood through the symmetrical stenosis model showing iv) blockage of flow at the stenosis region after minutes due to the formation of a blood clot (shown at higher magnification in the dotted box). D) i) Digital model of a simplified venous valve model and ii) a central lightsheet section of the printed construct showing the high-resolution leaflets (*) of the valve. iii,iv) Digital images of fluorescent beads perfused through the valve structure using a different fit of DLP-printed connectors, showing unidirectional flow (dotted lines show the outline of the printed construct and arrows indicate the direction of flow). Scale bars = 1 mm.

mechanical stability to the structure (Figure 7D(ii)). Next, we focused on providing a proof-of-concept demonstration of the possibility to perform volumetric printing across MEW meshes also in the presence of cells, with the capacity to pattern multiple cell-types, mimicking the structuring of blood vessels. For this, three distinct cellular layers were fabricated using the hybrid VolMEW approach. Native macroscale vessels, such as veins or arteries, have three distinct cell layers, the tunica intima, media, and externa, each consisting of different cell types (endothelial, smooth muscle, and fibroblasts, respectively) and matrix composition required for proper vessel function (Figure 7E). Our model tubular construct consisted of the previously described two-layer approach, but by adding a second VBP step with a new cell suspension (hMSCs, which have the capability to differentiate towards smooth muscle cells and fibroblasts, in the presence of the appropriate signals,^[73–75] labeled with a different fluorescent dye, DiI), an outer cell and material layer was successfully printed, creating a three-layer architecture that approximates the layered structure of a native vessel (Figure 7F,G).

Furthermore, the possibility of creating fenestrated, cellularized constructs was also demonstrated using the principles described in Figure 4. By first creating the first hydrogel layer as an inner print, leaving the outer edge of the vessel exposed, the second layer could still be printed within the MEW scaffold, leaving the small crossover points of the mesh exposed to the outside, creating the previously shown perfusable fenestrations in a cellularized model (Figure 7H). These final proof-of-principle prints demonstrate that the use of the VolMEW hybrid approach can be exploited in several ways to increase the complexity of current tissue-engineered macrovascular-inspired structures. While our experiments constitute a feasibility study for VolMEW as a bioprinting tool, future work aiming to produce fully functional vessels should first focus on extended culture time under flow to promote endothelial cell maturation, optimizing a proper tri-culture media system to either feed directly printed endothelial, smooth muscle cells and fibroblasts, or to induce the differentiation of MSCs into smooth muscle and fibroblastic phenotypes. Several biofabrication approaches have been

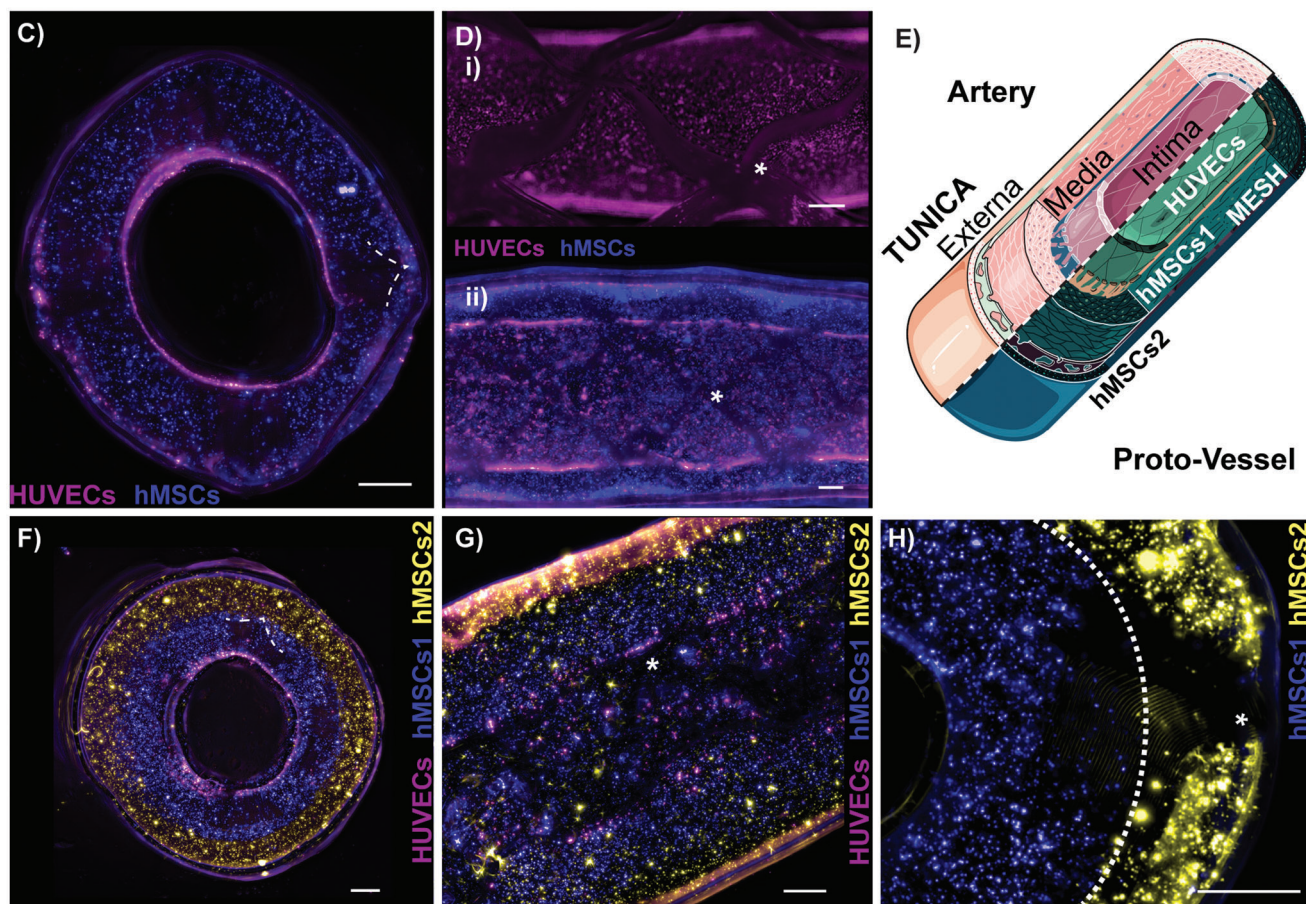
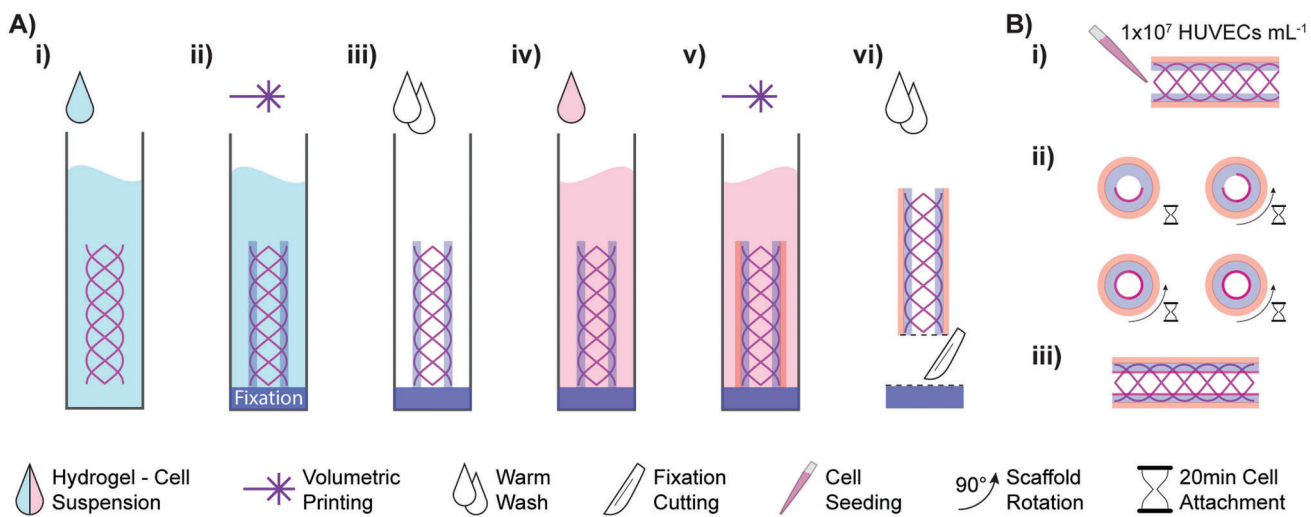


Figure 7. Sequential VolMEW printing of cell-laden, multi-material, and multi-layer tubular constructs. A) Graphical overview of the multi-material VolMEW printing process with cell-laden bioresins. i) The MEW mesh is inserted as previously described followed by ii) VBP of the scaffold with an overexposed fixation, whereby the construct is firmly attached to the printing vial. iii) After washing the residual, uncrosslinked hydrogel, iv,v) the process is repeated with the second material. Finally, the vi) fixation is cut with a scalpel. B) Depiction of the HUVEC seeding process, where first i) 1×10^7 cells mL^{-1} are pipetted into the construct, followed by ii) 20 min of incubation periods ending with 90° rotations. The process is repeated four times to homogeneously cover all sides to create iii) the final three-layer VolMEW construct. C) Perpendicular and D) ii) longitudinal cross-sectional fluorescence images of a two-layer VolMEW-printed tubular construct consisting of VBP-printed hMSCs (blue) in the gel layer encapsulating the MEW mesh. i) A HUVEC-seeded lumen (magenta) (dotted line represents the position of the MEW mesh crossover point). E) Diagram of native vessel structures compared to the VolMEW printed proto-vessels. F) Perpendicular and G) longitudinal cross-sectional fluorescence images of a three-layer VolMEW

explored to create architecturally complex vessels, including sacrificial extrusion templating,^[76,77] coaxial extrusion bioprinting,^[78] suspended bioprinting^[79] and suspended sacrificial printing,^[80] DLP printing,^[81–83] and acoustic wave patterning.^[84,85] Expanding on this toolkit, VolMEW introduces the ability to both tune the mechanical properties of the construct and to introduce custom-designed patterns of microfibers, which have been used in previous work to facilitate stromal cell alignment.^[31] Notably, and with broad applications beyond vascular-mimetic printing, VolMEW allows to freely sculpt the hydrogel component, creating features that intertwine with the MEW mesh, or, for example, incorporate fenestrations and branches relevant for hierarchical networks,^[86] and valve-like structures, of relevance to regulating flow and local pressure in vessels and more generally in fluidic components. While conventional approaches (i.e., casting) are still suitable when producing simple, single-component tubes, VolMEW does not require building and removing a physical mold, therefore facilitating the fabrication step, and improving precision. This facilitates the incorporation of complex structures within and around the reinforced tubes that would pose significant complications for casting procedures. Additionally, by printing with tomographic light patterns, hydrogel layers thinner than the reinforcing MEW mesh can be easily obtained, as shown in Figure 4. These architectures can be printed in seconds with no need for support materials, incorporating a mechanically reinforcing MEW mesh without compromising print resolution. Moreover, while this study focused on the advantage of producing mechanically competent grafts even when using soft hydrogels for tissue culture, previous literature provides consistent data that certain cell types, including different types of muscle cells, are able to align following the directionality of the MEW fibers, even when these are embedded in a hydrogel matrix.^[41,87,88] Future research on VolMEW could investigate this potential, for example, to guide cell orientation in vessels including, for example, a smooth muscle cell layer. Freedom of design in this contactless printing approach allows to produce architectures that cannot be easily obtained with other methods, and can therefore be potentially applied to produce patient-specific in vitro models, in which the effect of flow as a function of the (vascular) geometry, could be studied. This has implications, for instance, for systems to predict the kinetics of stenotic processes (in line with the proof of concept shown in Figure 6B,C), or even to produce personalized grafts for regenerative medicine. Overall, these features make VolMEW promising for the creation of next-generation tubular grafts with customizable designs that can be tailored to tissue-specific requirements and produced in high-throughput.

3. Conclusions

This study demonstrates, for the first time, the convergence of volumetric bioprinting with MEW to build geometrically complex

objects with enhanced mechanical properties, even when using low-stiffness bioresins commonly used in VP. In the first stage of the study, we presented the VolMEW setup, which takes advantage of the thermal gelation properties of gelMA and a custom-designed guide system to precisely place and align MEW constructs of different architectures. While the presence of MEW constructs in the VP vial is shown to attenuate the tomographic light path, VP-printed layers were successfully, and precisely sculpted onto and across the opaque microfibrillar meshes with high shape fidelity. Furthermore, the reinforcing effects observed in these converged printing constructs show mechanical advantages in flexural, burst, and tensile strength compared to non-reinforced scaffolds, reducing the gap between these hybrid biofabricated constructs and native tubular tissues of biological relevance, such as vascular structures. This newly developed approach also retains the high printing speeds (<20 s) and unparalleled design freedom associated with conventional VP. Exploiting this architectural freedom, an array of hierarchical, physiologically relevant constructs could be produced. This includes custom-designed and distributed wall fenestrations and complex printing of gyroid-structures, bifurcated channels, and a functional venous valve model within the reinforced hydrogel tubes. As a proof-of-concept, the possibility of creating multi-material and multi-cellular structures through a sequential printing approach was also demonstrated. The three distinct layers found in native macro-vessels (i.e., veins and arteries) could be replicated in these reinforced, composite structures, demonstrating the potential to create hierarchical living constructs with the VolMEW approach. Notably, since the MEW meshes can be bulk produced and stored for printing, future applications can be envisioned, in which off-the-shelf mesh geometries could be readily loaded into a volumetric printer, to add the hydrogel and cellular components just before their intended application. Overall, this novel technique poses the possibility of creating volumetric composite objects from materials with very different chemical and physical properties (hydrogels and thermoplastics) with enhanced mechanical properties and high design freedom. By leveraging the advantages of the MEW and VP technologies in the present approach, these findings also provide exciting opportunities for future hybrid applications with other opaque materials (i.e., ceramics, metals) for advanced tissue engineering strategies.

4. Experimental Section

Materials: For MEW, medical-grade polycaprolactone (PCL) (PURA-SORB PC 12, Corbion Inc., Gorinchem, The Netherlands) was used to fabricate the MEW tubular scaffolds. As a bioresin for volumetric (bio)printing, gelatin methacryloyl (93.5% DoF) was synthesized as previously reported^[89] and used as 5% w/v (cellular experiments), 15% w/v (venous valve), and 8% w/v (all others) solution in phosphate-buffered saline (PBS). As photoinitiator, 0.1% w/v lithium phenyl(2,4,6-trimethylbenzoyl)phosphinate (LAP, Tokyo Chemical Industry, Japan) was supplemented to the hydrogel precursor solution to initiate the photocrosslinking reaction.

printed tubular construct consisting of VBP-printed hMSCs (blue and yellow) in the gel layer encapsulating the MEW mesh and a HUVEC-seeded lumen (magenta). H) Sequentially printed multi-material construct with crossover points exposed, embedding the MEW mesh in both layers (asterisk represents the MEW mesh crossover point tip, and dotted line represents the separation between printed cell layers). (E) was partly generated using Servier Medical Art, provided by Servier, licensed under a CC-BY Creative Commons Attribution 3.0 unported license (<https://creativecommons.org/licenses/by/3.0/>). Scale bars = 500 μm.

Melt Electrowriting of Tubular Structures with Different Geometries: Tubular MEW constructs were processed using two custom-made MEW devices with a cylindrical and interchangeable collector. One device, used to fabricate tensile test specimens, employed an Aerotech axis system (PRO115) and the A3200 (Aerotech, USA) software suite as coding and machine operating interface. Polypropylene cartridges, and 22G flat-tip needles (Nordson EFD, USA) were used. The second device, used for all other experiments, has been described elsewhere^[28] and was used with an electrically heated 3 mL glass syringe and a 25G needle. A modified code was developed similar to previous work,^[25] to move the collector in translational and rotational directions for precise fiber placement onto a rotating steel mandrel at predetermined winding angles.

Thermally Controlled Incorporation of Tubular MEW Meshes into Volumetric Printing Setup: In order to insert the tubular MEW scaffolds in a perfectly centered and reproducible manner, the scaffolds were transferred to 3 mm pultruded carbon fiber rods (easycomposites, The Netherlands) matching the inner diameter of the MEW mesh. To center the rod inside a Ø10 mm cylindrical borosilicate glass vial compatible for use with the volumetric printer, small inserts were printed on a Perfactory 3 DLP 3D printer (Envisontec, Germany) using PIC100 resin to fit the rod and perfectly match the inner diameter of the vial. To fix the samples in the center of the vial, the tubular mesh was placed on the end of the insertion rod with a 5 mm offset. The printing vial was then filled with preheated (37 °C) bioresin and the rod was inserted. The vial was subsequently placed in ice water up to the beginning of the insertion rod until gelation occurred. The gelled bioresin held the tubular mesh firmly in place. The insertion rod was raised to the upper limit of the tubular mesh and the gelation process was repeated, resulting in a centered sample.

Volumetric (Bio)Printing Process: A commercial Tomolite v1.0 (Readily3D SA, Switzerland) volumetric printing setup was used to fabricate the hybrid VolMEW constructs. The gelMA bioresin-infused MEW meshes were prepared as described above in Ø10 mm cylindrical borosilicate glass vials and kept cool at 4 °C to ensure that the resin remained thermally gelled. Custom-designed CAD files (Fusion360) were loaded and processed using the Readily3D Apparite software (b11409a). The average light intensity across all prints was set at 12.16 mW cm⁻². Venous valve models were additionally printed using Apparite's proprietary settings for a bulk length of 400 µm and a bulk multiplier of 2x. After printing, the thermally gelled bioresin was gently washed with pre-warmed PBS at 37 °C to remove the uncrosslinked resin from the printed structure. To achieve homogeneous crosslinking and facilitate sample handling, the samples were immersed in a 0.01% w/v LAP solution and post-cured for 5 min in a UV oven (CI-1000, Ultraviolet Crosslinker, λ = 365 nm, I = 8 mW cm⁻² UVP, USA). All printed structures for mechanical analysis and complex geometries were printed at a gelMA concentration of 8% w/v, except for the venous valve model. For this structure, a 15% w/v GelMA concentration was selected for the sake of visualization and handling, as stiffer hydrogels provided higher yield strength of the printed leaflets, and therefore withstood higher pressures when the flow was directed against the closed valve. All cell-laden constructs were printed at a gelMA concentration of 5% w/v.

Measurements of MEW Mesh Light Attenuation Effect during VP: Tubular MEW meshes were placed in cylindrical vials containing the gelMA resin. The vials were then placed within the print area of the volumetric printer and coupled to the rotary stage (Newmark RB-90). Index matching was achieved by immersing the vial in a square cuvette containing distilled water. A virtual beam was generated by encoding a circular region of on-sate pixels on a DMD (Vialux Hi-Speed V-7000) illuminated by a collimated 520 nm source. This corresponded to a beam waist diameter of 200 ± 10 µm. The vial was positioned so that the virtual beam was incident on the central axis of the embedded MEW mesh and the vial. A biased photodetector (Thorlabs DET36A2) was positioned 100 ± 5 mm behind the vial and was used to measure the relative intensity of the incident light after attenuation by the scaffold. A digital acquisition board (National Instruments USB-6001) was used to acquire the voltage signal from the photodiode. In order to perform the measurement, the virtual beam was turned on and the vial was rotated at a rate of 36° s⁻¹ over a full rotation. The resulting voltage signal from the photodiode was recorded at a

sampling rate of 50 Hz. For each sample, this measurement was acquired at 3 locations on the MEW mesh, with the virtual beam being offset by +3 and -3 mm from its central position. The acquired data was normalized with 100% being the maximum amount of light detected across all runs. The runs were then rotated to start at the first peak using Savitzky–Golay filtering, followed by finding the first local maximum, and the resulting phase-matched raw data were averaged using time synchronous averaging (Matlab R2022a). The area under the curve was approximated using discrete trapezoidal numerical integration and the data were normalized (deg) and plotted (Matlab R2022a).

Tensile Testing of Hybrid VolMEW Constructs: To determine the radial mechanical properties of the VolMEW constructs, a customized two-pin mounting setup was used on a dynamic mechanical tester (Electron-Force 5500, TA Instruments, USA). Two metal pins were inserted through the luminal cavity of the constructs and a radial tensile force was applied during the test procedure (Figure 3A). Samples were measured in a 100-cycle waveform setup with a peak displacement of 18% strain with respect to the inner tube diameter. Construct measurements were evaluated after the initial hysteresis had subsided and the peak force had stabilized over several cycles. A second evaluation was a pull to 166% strain to elucidate the maximum stress values beyond physiological values of small-diameter blood vessels. For comparison, porcine arteries were also tested. Porcine coronary arteries were procured directly from a local butcher as full hearts and subsequently dissected from them. They were stored at -20 °C until the day of measurement, where they were thawed at room temperature before being mounted onto the mechanical testing setup.

Burst Pressure Analysis of VolMEW Constructs: A Vieweg DC 200 (Vieweg, Germany) dispenser, which uses pressurized air to dispense material, was used with a custom tubing array that included a pressure gauge for readout and a Luer connector to a custom-made bioreactor assembly part created by DLP printing on a Prusa SL1s resin printing system (Prusa, Czech Republic) with Dreve FotoDent guide 405 nm (Dreve, Germany). The resin was also used to fix VolMEW constructs liquid tight into the assembly part, a thin cover of FotoDent has been applied to the connectors and cured with a Prusa CW1 curing and washing station (Prusa, Czech Republic). Vaseline was then injected into the VolMEW construct through an attached printer cartridge (Nordson, USA) until the construct's lumen was completely filled with Vaseline. The opposing end of the assembly was then sealed off and air pressure was applied via the printer cartridge by the dispenser until failure of the constructs could be observed by Vaseline breaking through the construct. Data collection was done by digital video recording of VolMEW constructs consisting of MEW meshes of different architectures and number of layers.

Bending Resistance Evaluation of VolMEW Constructs: To evaluate the effect of MEW mesh incorporation on the bending resistance of the hydrogel constructs, 27.5 mm long VolMEW scaffolds were printed with meshes of rhombic pores with 34° winding angle consisting of different layer numbers (0, 20, 40, and 60). Based on the previously established filament collapse test developed to evaluate the shape fidelity of bioinks^[57] similar 5 mm column structures were printed from polylactic acid (PLA, Maker-Point) using a fused deposition modeling printer (Ultimaker S3, Ultimaker, The Netherlands) with gaps of 25, 20, 16, 12, 8, and 4 mm, to assess the maximum deformation of the printed structures as they spanned each gap distance. Maximum deformation was measured as the lowest point the sample bent downwards from the top of the column structure.

Blood Clotting Assay in Symmetric Stenosis Model: Equine blood was collected in 3.2% citrated tubes at the Horse Clinic, Faculty of Veterinary Medicine, Utrecht University, as a redundant sample from veterinary surgery practice, in accordance to the institutional ethical committee of Utrecht University. Citrate prevented blood from clotting immediately after extraction. To allow blood to clot again it needed to be recalcified previous to the experiment. The recalcification buffer consisted of 63.2 mM CaCl₂ and 31.6 mM MgCl₂. Tubing used for blood perfusion was coated in a 200 mM CaCl₂, 0.1 µL mL⁻¹ Heparin, 1% BSA, and 1% Glucose in HEPES solution overnight to prevent the blood from clotting in it. Blood was continuously perfused through the symmetric stenosis model at a flow rate of 0.58 mL min⁻¹ using a syringe pump (AL-2000, World Precision Instruments). The tubes were perfused for 10 min or until blockage

was observed due to blood clotting. Videos and images of the perfused model were acquired with an Olympus SZ61 stereomicroscope coupled with an Olympus DP70 digital camera (Olympus Soft Imaging Solutions GmbH, The Netherlands).

Cell Isolation and Culture: Green fluorescent human umbilical vein endothelial cells (GFP-HUVECs; cAP-001GFP, Angioproteomie) were expanded in type I collagen precoated culture flasks in endothelial cell growth medium-2 (EGM-2) BulletKit medium (CC-3162, Lonza). Culture flasks were precoated with 50 $\mu\text{g mL}^{-1}$ collagen I rat tail (354236, Corning) in 0.01 M HCl for 1 h at 37 °C, followed by two washes with PBS. GFP-HUVECs were used in experiments at passages 6–7 and cultured in EGM-2 medium for expansion and differentiation. Human bone-marrow-derived mesenchymal stromal cells (hbMSCs) were isolated from bone marrow aspirates of consenting patients, as previously described.^[90] Briefly, human bone marrow aspirates were obtained from the iliac crest of patients that were receiving spondylodesis or hip replacement surgery. Isolation and distribution were performed in accordance with protocols approved by the Biobank Research Ethics Committee (isolation 08-001, distribution protocol 18–739, University Medical Center Utrecht). Protocols used were in line with the principles embodied in the Declaration of Helsinki. HbMSCs were expanded in DMEM + GlutaMAX supplemented with FBS (10% v/v) and p/s 1%. The procedures for human tissue and cell isolation were approved by the Research Ethics Committee of the University Medical Center Utrecht.^[90] All cells were cultured at 37 °C, 5% CO₂, and used at passages 4–5.

Volumetric Bioprinting of Reinforced Multilayered MacrovesSEL-Like Structures: Mechanically reinforced macrovesSEL structures mimicking the layered structure of native vessels (tunica intima, media, and externa) were fabricated using a sequential bioprinting approach. The following procedure was used to fabricate two- and three-layer protovesSEL constructs. First, a 15 mm hybrid VolMEW hollow tube was printed with 1×10^6 cells mL^{-1} hbMSCs labeled with membrane staining DiD (ThermoFisher Scientific, The Netherlands) encapsulated in 5% w/v gelMA + 0.1% w/v LAP bioresin. In this first layer, a MEW scaffold (40 layers) with rhombic pores of 34° winding angle and 8 pivot points was incorporated and completely encapsulated by the printed gel layer of 1050 μm . For the 3-layer structure, the sample was washed after the first printing step and re-infused in a bioresin suspension containing 5×10^5 cells mL^{-1} hbMSCs labeled with membrane staining DiI (ThermoFisher Scientific, The Netherlands), and a second outer layer of 800 μm was printed around the first cell layer. Samples were washed, post-cured for 5 min, and cultured in hbMSC expansion medium overnight. The next day, the samples were placed on a rectangular mold with a concave slot for the tube to rest on, and the channels were seeded with a suspension of 1×10^7 cells mL^{-1} GFP-HUVECs. Samples were rotated 90° every 20 min, for a total span of 80 min to achieve homogeneous cell seeding across the lumen of the tubular structure. To create a fenestrated 3-layer tubular structure, the same protocol was used, but the total width of the two cell layers was reduced to allow for overprinting of the MEW mesh outside the gel sample. Lateral and longitudinal cross-sections of the samples were imaged after 7 days of culture in EGM-2 BulletKit medium using a Thunder imaging system (Leica Microsystems, Germany).

Statistical Analyses: Results were reported as mean \pm standard deviation (S.D.). Statistical analysis was performed using GraphPad Prism 9.0 (GraphPad Software, USA). For tensile test results, Origin 2022 (OriginLab, USA) was used. Comparisons between experimental groups were assessed via one or two-way ANOVAs, followed by post hoc Bonferroni correction to test differences between groups. Non-parametric tests were used when normality could not be assumed. Differences were considered significant when $p < 0.05$. Significance was expressed on graphs as follows: * $p < 0.05$, ** $p < 0.01$, *** $p < 0.001$, **** $p < 0.0001$.

Supporting Information

Supporting Information is available from the Wiley Online Library or from the author.

Acknowledgements

G.G., M.B.K., C.G., and P.N.B. contributed equally to this work. T.J. and R.L. share correspondence. The authors would like to acknowledge Lisa Galaba, Sven Heilig, Philipp Stahlhut, Marième Gueye and Marta Foronda García for their support in the experimental activities. This project received funding from the European Research Council (ERC) under the European Union's Horizon 2020 research and innovation programme (grant agreement No. 949806, VOLUME-BIO), and from the European Union's Horizon 2020 research and innovation programme under grant agreement No. 964497 (ENLIGHT). R.L. and J.M. acknowledge the funding from the ReumaNederland (LLP-12, LLP22, and 19-1-207 MINIJOINT). M.d.R., R.L., and J.M. acknowledge the funding from the Gravitation Program "Materials Driven Regeneration", funded by the Netherlands Organization for Scientific Research (024.003.013). R.L. also acknowledges funding from the NWA-Ideëengenerator programme of the Netherlands Organization for Scientific Research (NWA.1228.192.105). M.B.K. and T.J. would like to thank the German Research Foundation (DFG, Project No. 326998133-TRR 225 – subproject B09) for financial support. The DFG also supported the project with a "State Major Instrumentation Programme" (INST 105022/58-1 FUGG) that enabled SEM analysis of the samples. Further, M.B.K., C.G., J.G., and T.J. thank the European Union for support on printing strategies (European Fund for Regional Development – EFRE Bayern, Bio3D-Druck project 20-3400-2-10). T.J. acknowledges the European Union for funding via the European Union's Horizon 2020 research and innovation program (BRAVE) under Grant Agreement No. 874827.

Conflict of Interest

R.L. is scientific advisor for Readily3D SA, which did not participate in or bias the work. The other authors declare no conflict of interest.

Data Availability Statement

The data that support the findings of this study are available from the corresponding author upon reasonable request.

Keywords

biofabrication, bioprinting hydrogels, melt electrowriting, volumetric additive manufacturing

Received: January 24, 2023
Revised: April 17, 2023
Published online: June 22, 2023

- [1] R. Levato, T. Jungst, R. G. Scheuring, T. Blunk, J. Groll, J. Malda, *Adv. Mater.* **2020**, *32*, 1906423.
- [2] J. Groll, J. A. Burdick, D. W. Cho, B. Derby, M. Gelinsky, S. C. Heilshorn, T. Jungst, J. Malda, V. A. Mironov, K. Nakayama, A. Ovsianikov, W. Sun, S. Takeuchi, J. J. Yoo, T. B. F. Woodfield, *Biofabrication* **2019**, *11*, 013001.
- [3] K. S. Lim, R. Levato, P. F. Costa, M. D. Castilho, C. R. Alcalá-Orozco, K. M. A. Van Dorenmalen, F. P. W. Melchels, D. Gawlitta, G. J. Hooper, J. Malda, T. B. F. Woodfield, *Biofabrication* **2018**, *10*, 034101.
- [4] F. P. W. Melchels, J. Feijen, D. W. Grijpma, *Biomaterials* **2010**, *31*, 6121.
- [5] H. W. Kang, S. J. Lee, I. K. Ko, C. Kengla, J. J. Yoo, A. Atala, *Nat. Biotechnol.* **2016**, *34*, 312.
- [6] S. L. Ding, X. Liu, X. Y. Zhao, K. T. Wang, W. Xiong, Z. L. Gao, C. Y. Sun, M. X. Jia, C. Li, Q. Gu, M. Z. Zhang, *Bioact. Mater.* **2022**, *17*, 81.
- [7] N. V. Mekhileri, K. S. Lim, G. C. J. Brown, I. Mutreja, B. S. Schon, G. J. Hooper, T. B. F. Woodfield, *Biofabrication* **2018**, *10*, 024103.

- [8] A. C. Daly, D. J. Kelly, *Biomaterials* **2019**, 197, 194.
- [9] M. Nakamura, A. Kobayashi, F. Takagi, A. Watanabe, Y. Hiruma, K. Ohuchi, Y. Iwasaki, M. Horie, I. Morita, S. Takatani, *Tissue Eng.* **2005**, 11, 1658.
- [10] P. D. Dalton, *Curr. Opin. Biomed. Eng.* **2017**, 2, 49.
- [11] T. M. Robinson, D. W. Hutmacher, P. D. Dalton, *Adv. Funct. Mater.* **2019**, 29, 1904664.
- [12] M. Castilho, M. de Ruijter, S. Beirne, C. C. Villette, K. Ito, G. G. Wallace, J. Malda, *Trends Biotechnol.* **2020**, 38, 1316.
- [13] M. Tavafoghi, M. A. Darabi, M. Mahmoodi, R. Tutar, C. Xu, A. Mirjafari, F. Billi, W. Swieszkowski, F. Nasrollahi, S. Ahadian, V. Hosseini, A. Khademhosseini, N. Ashammakhi, *Biofabrication* **2021**, 13, 042002.
- [14] P. N. Bernal, P. Delrot, D. Loterie, Y. Li, J. Malda, C. Moser, R. Levato, *Adv. Mater.* **2019**, 31, 1904209.
- [15] D. Loterie, P. Delrot, C. Moser, *Nat. Commun.* **2020**, 11, 852.
- [16] T. Zandrini, S. Florczak, R. Levato, A. Ovsianikov, *Trends Biotechnol.* **2022**, 41, 604.
- [17] J. Visser, F. P. W. Melchels, J. E. Jeon, E. M. Van Bussel, L. S. Kimpton, H. M. Byrne, W. J. A. Dhert, P. D. Dalton, D. W. Hutmacher, J. Malda, *Nat. Commun.* **2015**, 6, 6933.
- [18] T. D. Brown, P. D. Dalton, D. W. Hutmacher, *Prog. Polym. Sci.* **2016**, 56, 116.
- [19] N. Abbasi, A. Abdal-Hay, S. Hamlet, E. Graham, S. Ivanovski, *ACS Biomater. Sci. Eng.* **2019**, 5, 3448.
- [20] M. Castilho, G. Hochleitner, W. Wilson, B. Van Rietbergen, P. D. Dalton, J. Groll, J. Malda, K. Ito, *Sci. Rep.* **2018**, 8, 1245.
- [21] J. C. Kade, P. D. Dalton, *Adv. Healthcare Mater.* **2021**, 10, 2001232.
- [22] R. Sanchez Diaz, J. R. Park, L. L. Rodrigues, P. D. Dalton, E. M. De-Juan-Pardo, T. R. Dargaville, *Adv. Mater. Technol.* **2021**, 7, 2100508.
- [23] M. J. Ainsworth, O. Lotz, A. Gilmour, A. Zhang, M. J. Chen, D. R. McKenzie, M. M. Bilek, J. Malda, B. Akhavan, M. Castilho, *Adv. Funct. Mater.* **2022**, 33, 2206583.
- [24] M. Castilho, R. Levato, P. N. Bernal, M. De Ruijter, C. Y. Sheng, J. Van Duijn, S. Piluso, K. Ito, J. Malda, *Biomacromolecules* **2021**, 22, 855.
- [25] E. McColl, J. Groll, T. Jungst, P. D. Dalton, *Mater. Des.* **2018**, 155, 46.
- [26] T. Jungst, M. L. Muerza-Cascante, T. D. Brown, M. Standfest, D. W. Hutmacher, J. Groll, P. D. Dalton, *Polym. Int.* **2015**, 64, 1086.
- [27] T. D. Brown, A. Slotosch, L. Thibaudeau, A. Taubenberger, D. Loessner, C. Vaquette, P. D. Dalton, D. W. Hutmacher, *Biointerphases* **2012**, 7, 13.
- [28] A. M. van Genderen, K. Jansen, M. Kristen, J. van Duijn, Y. Li, C. C. L. Schuurmans, J. Malda, T. Vermonden, J. Jansen, R. Masereeuw, M. Castilho, *Front. Bioeng. Biotechnol.* **2021**, 8, 617364.
- [29] Z. Qiao, M. Lian, Y. Han, B. Sun, X. Zhang, W. Jiang, H. Li, Y. Hao, K. Dai, *Biomaterials* **2021**, 266, 120385.
- [30] F. Afghah, N. B. Iyison, A. Nadernezhad, A. Midi, O. Sen, B. Saner Okan, M. Culha, B. Koc, *Adv. Healthcare Mater.* **2022**, 11, 2102068.
- [31] T. Jungst, I. Pennings, M. Schmitz, A. J. W. P. Rosenberg, J. Groll, D. Gawlitta, *Adv. Funct. Mater.* **2019**, 29, 1905987.
- [32] M. de Ruijter, A. Ribeiro, I. Dokter, M. Castilho, J. Malda, *Adv. Healthcare Mater.* **2019**, 8, 1800418.
- [33] P. N. Bernal, M. Bouwmeester, J. Madrid-Wolff, M. Falandt, S. Florczak, N. G. Rodriguez, Y. Li, G. Größbacher, R. A. Samsom, M. van Wolferen, L. J. W. van der Laan, P. Delrot, D. Loterie, J. Malda, C. Moser, B. Spee, R. Levato, *Adv. Mater.* **2022**, 34, 2110054.
- [34] M. Bartnikowski, T. R. Dargaville, S. Ivanovski, D. W. Hutmacher, *Prog. Polym. Sci.* **2019**, 96, 1.
- [35] N. Golafshan, E. Vorndran, S. Zaharievski, H. Brommer, F. B. Kadumudi, A. Dolatshahi-Pirouz, U. Gbureck, R. van Weeren, M. Castilho, J. Malda, *Biomaterials* **2020**, 261, 120302.
- [36] P. Diloksumpan, F. Abinzano, M. de Ruijter, A. Mensinga, S. Plomp, I. Khan, H. Brommer, I. Smit, M. Dias Castilho, P. R. van Weeren, J. Malda, R. Levato, *J. Trial Error* **2021**, 2, 7.
- [37] A. Daghery, J. A. Ferreira, J. Xu, N. Golafshan, D. Kaigler, S. B. Bhaduri, J. Malda, M. Castilho, M. C. Bottino, *Bioact. Mater.* **2023**, 19, 268.
- [38] B. E. Kelly, I. Bhattacharya, H. Heidari, M. Shusteff, C. M. Spadaccini, H. K. Taylor, *Science* **2019**, 363, 1075.
- [39] R. Rizzo, D. Ruetsche, H. Liu, M. Zenobi-Wong, *Adv. Mater.* **2021**, 33, 2102900.
- [40] J. Gehlen, W. Qiu, G. N. Schädli, R. Müller, X. H. Qin, *Acta Biomater.* **2022**, 156, 49.
- [41] M. Castilho, A. van Mil, M. Maher, C. H. G. Metz, G. Hochleitner, J. Groll, P. A. Doevendans, K. Ito, J. P. G. Sluijter, J. Malda, *Adv. Funct. Mater.* **2018**, 28, 1803151.
- [42] D. B. Camasão, D. Mantovani, *Mater Today Bio* **2021**, 10, 100106.
- [43] J. Schöneberg, F. De Lorenzi, B. Theek, A. Blaeser, D. Rommel, A. J. C. Kuehne, F. Kießling, H. Fischer, *Sci. Rep.* **2018**, 8, 10430.
- [44] P. Zilla, D. Bezuidenhout, P. Human, *Biomaterials* **2007**, 28, 5009.
- [45] M. Stekelenburg, M. C. M. Rutten, L. H. E. H. Snoeckx, F. P. T. Baaijens, *Tissue Eng., Part A* **2009**, 15, 1081.
- [46] X. Li, H. Zhao, *J. Biomater. Appl.* **2019**, 33, 1017.
- [47] C. M. Brennan, K. F. Eichholz, D. A. Hoey, *Biomed. Mater.* **2019**, 14, 065016.
- [48] A. B. McCosker, M. E. Snowdon, R. Lamont, M. A. Woodruff, N. C. Paxton, *Adv. Mater. Technol.* **2022**, 7, 2200259.
- [49] E. Pickering, N. C. Paxton, A. Bo, B. O'Connell, M. King, M. A. Woodruff, *Adv. Eng. Mater.* **2022**, 24, 2200479.
- [50] V. Kasjanovs, I. Ozolanta, B. Purina, *Mech. Compos. Mater.* **1999**, 35, 155.
- [51] T. D. Brown, P. D. Dalton, D. W. Hutmacher, *Adv. Mater.* **2011**, 23, 5651.
- [52] G. Hochleitner, T. Jungst, T. D. Brown, K. Hahn, C. Moseke, F. Jakob, P. D. Dalton, J. Groll, *Biofabrication* **2015**, 7, 035002.
- [53] N. Pien, M. Bartolf-Kopp, L. Parmentier, J. Delaey, L. De Vos, D. Mantovani, S. Van Vlierberghe, P. Dubruel, T. Jungst, *Macromol. Mater. Eng.* **2022**, 307, 2200097.
- [54] N. Diban, S. Haimi, L. Bolhuis-Versteeg, S. Teixeira, S. Miettinen, A. Poot, D. Grijpma, D. Stamatialis, *Acta Biomater.* **2013**, 9, 6450.
- [55] V. Thomas, X. Zhang, Y. K. Vohra, *Biotechnol. Bioeng.* **2009**, 104, 1025.
- [56] K. W. M. Boere, J. Visser, H. Seyednejad, S. Rahimian, D. Gawlitta, M. J. Van Steenbergen, W. J. A. Dhert, W. E. Hennink, T. Vermonden, J. Malda, *Acta Biomater.* **2014**, 10, 2602.
- [57] A. Ribeiro, M. M. Blokzijl, R. Levato, C. W. Visser, M. Castilho, W. E. Hennink, T. Vermonden, J. Malda, *Biofabrication* **2018**, 10, 014102.
- [58] C. Xie, Q. Gao, P. Wang, L. Shao, H. Yuan, J. Fu, W. Chen, Y. He, *Mater. Des.* **2019**, 181, 108092.
- [59] W. G. Roberts, G. E. Palade, *Cancer Res.* **1997**, 57, 765.
- [60] S. C. Satchell, F. Braet, *Am. J. Physiol. Renal. Physiol.* **2009**, 296, F947.
- [61] J. Bernier-Latmani, C. Mauri, R. Marcone, F. Renevey, S. Durot, L. He, M. Vanlandewijck, C. Maclachlan, S. Davanture, N. Zamboni, G. W. Knott, S. A. Luther, C. Betsholtz, M. Delorenzi, C. Brisken, T. V. Petrova, *Nat. Commun.* **2022**, 13, 3983.
- [62] G. Grevers, U. Herrmann, *Arch Otorhinolaryngol* **1987**, 244, 55.
- [63] S. Parab, R. E. Quick, R. L. Matsuoka, *Elife* **2021**, 10, e64295.
- [64] F. Benz, S. Liebner, *Physiology, Pharmacology and Pathology of the Blood-Brain Barrier*, (Eds.: Z. Cader, W. Neuhaus), Springer Nature, Cham, Switzerland **2020**, pp. 3–31.
- [65] M. Kaya, L. Chang, A. Truong, M. W. Brightman, *Exp. Neurol.* **1996**, 142, 6.
- [66] P. A. Stewart, K. Hayakawa, E. Hayakawa, C. L. Farrell, R. F. Del Maestro, *Acta Neuropathol.* **1985**, 67, 96.
- [67] T. F. Browne, D. Hartley, S. Purchas, M. Rosenberg, G. Van Schie, M. Lawrence-Brown, *Eur. J. Vasc. Endovasc. Surg.* **1999**, 18, 445.
- [68] P. M. Bungay, N. Burfitt, K. Sritharan, L. Muir, S. L. Khan, M. C. De Nunzio, K. Lingam, A. H. Davies, *J. Vasc. Surg.* **2011**, 54, 1832.

- [69] B. M. Stanley, J. B. Semmens, M. Lawrence-Brown, M. A. Goodman, D. E. Hartley, *J. Endovasc. Ther.* **2001**, *8*, 16.
- [70] W. J. Kim, G. H. Kim, *Theranostics* **2020**, *10*, 2495.
- [71] M. Gallois, T. Gidenne, L. Fortun-Lamothe, I. L. Huerou-Luron, J. P. Lallès, *Reprod., Nutr., Dev.* **2005**, *45*, 109.
- [72] R. Abbasi, T. B. Lefevre, A. D. Benjamin, I. J. Thornton, J. N. Wilking, *Lab Chip* **2021**, *21*, 2050.
- [73] T. Wang, Z. Xu, W. Jiang, A. Ma, *Int. J. Cardiol.* **2006**, *109*, 74.
- [74] K. Kurpinski, H. Lam, J. Chu, A. Wang, A. Kim, E. Tsay, S. Agrawal, D. V. Schaffer, S. Li, *Stem Cells* **2010**, *28*, 734.
- [75] A. Augello, C. De Bari, *Hum. Gene Ther.* **2010**, *21*, 1226.
- [76] D. B. Kolesky, K. A. Homan, M. A. Skylar-Scott, J. A. Lewis, *Proc. Natl. Acad. Sci. USA* **2016**, *113*, 3179.
- [77] L. Ouyang, J. P. K. Armstrong, Q. Chen, Y. Lin, M. M. Stevens, *Adv. Funct. Mater.* **2020**, *30*, 1908349.
- [78] L. Shao, Q. Gao, C. Xie, J. Fu, M. Xiang, Y. He, *Biofabrication* **2020**, *12*, 035014.
- [79] C. Dikyol, M. Altunbek, B. Koc, *J. Mater. Res.* **2021**, *36*, 3851.
- [80] M. A. Skylar-Scott, S. G. M. Uzel, L. L. Nam, J. H. Ahrens, R. L. Truby, S. Damaraju, J. A. Lewis, *Sci. Adv.* **2019**, *5*, eaaw2459.
- [81] R. Levato, K. S. Lim, W. Li, A. U. Asua, L. B. Peña, M. Wang, M. Falandt, P. N. Bernal, D. Gawlitta, Y. S. Zhang, T. B. F. Woodfield, J. Malda, *Mater Today Bio* **2021**, *12*, 100162.
- [82] W. Zhu, X. Qu, J. Zhu, X. Ma, S. Patel, J. Liu, P. Wang, C. S. E. Lai, M. Gou, Y. Xu, K. Zhang, S. Chen, *Biomaterials* **2017**, *124*, 106.
- [83] B. Grigoryan, S. J. Paulsen, D. C. Corbett, D. W. Sazer, C. L. Fortin, A. J. Zaita, P. T. Greenfield, N. J. Calafat, J. P. Gounley, A. H. Ta, F. Johansson, A. Randles, J. E. Rosenkrantz, J. D. Louis-Rosenberg, P. A. Galie, K. R. Stevens, J. S. Miller, *Science* **2019**, *364*, 458.
- [84] D. Petta, V. Basoli, D. Pellicciotta, R. Tognato, J. Barcik, C. Arrigoni, E. D. Bella, A. R. Armiento, C. Candrian, R. G. Richards, M. Alini, M. Moretti, D. Eglin, T. Serra, *Biofabrication* **2020**, *13*, 015004.
- [85] B. Kang, J. Shin, H. J. Park, C. Rhyou, D. Kang, S. J. Lee, Y. S. Yoon, S. W. Cho, H. Lee, *Nat. Commun.* **2018**, *9*, 5402.
- [86] L. de Silva, P. N. Bernal, A. J. W. Rosenberg, J. Malda, R. Levato, D. Gawlitta, *Acta Biomater.* **2022**, *156*, 250.
- [87] M. Castilho, D. Feyen, M. Flandes-Iparraguirre, G. Hochleitner, J. Groll, P. A. F. Doevendans, T. Vermonden, K. Ito, J. P. G. Sluijter, J. Malda, *Adv. Healthcare Mater.* **2017**, *6*, 1700311.
- [88] G. Cedillo-Servin, O. Dahri, J. Meneses, J. van Duijn, F. Sage, J. Silva, A. Pereira, F. D. Magalhães, J. Malda, N. Geijsen, M. Castilho, *bioRxiv* **2017**, <https://doi.org/10.1101/2023.01.19.524679>.
- [89] K. S. Lim, F. Abinzano, P. N. Bernal, A. Albillos Sanchez, P. Atienza-Roca, I. A. Otto, Q. C. Peiffer, M. Matsusaki, T. B. F. Woodfield, J. Malda, R. Levato, *Adv. Healthcare Mater.* **2020**, *9*, 1901792.
- [90] M. L. Terpstra, J. Li, A. Mensinga, M. De Ruijter, M. H. P. Van Rijen, C. Androulidakis, C. Galiotis, I. Papantoniou, M. Matsusaki, J. Malda, R. Levato, *Biofabrication* **2022**, *14*, 034104.